

Supplementary Information

**The projected future degradation in air quality is caused by more abundant
natural aerosols in a warmer world**

James Gomez and Robert J. Allen

Department of Earth and Planetary Sciences, University of California Riverside, CA, USA

Steven T. Turnock

Met Office Hadley Centre, Exeter, UK

Larry W. Horowitz and Paul Ginoux

NOAA/OAR Geophysical Fluid Dynamics Laboratory, Princeton, New Jersey, USA

Kostas Tsigaridis and Susanne E. Bauer

Center for Climate Systems Research, Columbia University, NASA Goddard Institute for Space
Studies, New York, NY, USA

Dirk Olivié

Norwegian Meteorological Institute, Oslo, Norway

Erik S. Thomson

Department of Chemistry and Molecular Biology, Atmospheric Science, University of Gothenburg,
Gothenburg, Sweden

Contents of this file

Supplementary Note 1: Linearity of the PM_{2.5} Response

Supplementary Note 2: Additional Details on the Sea Salt Response

Supplementary Note 3: Wet Removal Efficiency

Supplementary Note 4: UKESM1-0-LL Saharan Dust Response

Supplementary Note 5: GISS-E2-1-G OMA versus MATRIX

Supplementary Note 6: Isoprene Emission Responses

Supplementary Note 7: Archived versus Approximated PM_{2.5}

Supplementary Note 8: Alternative PM_{2.5} Approximation (0.3 DU Factor)

Supplementary Note 9: Fire Responses to Increasing CO₂ and Warming

Figures S1 to S16

Tables S1 to S2

Supplementary References

Supplementary Note 1: Linearity of the PM_{2.5} Response

Although the PM_{2.5} changes are in response to a large perturbation (global annual mean warming is 3.8 ± 0.4 K), the warming is comparable to end-of-21st century warming (relative to 1850-1900) under the high emissions, low mitigation future scenario SSP3-7.0. Moreover, we find that PM_{2.5} increases linearly with global mean temperature (Supplementary Figure 1). All but one model yields a significant global mean correlation coefficient (over 140 years of the 1% per year CO₂ simulation) between PM_{2.5} and surface temperature. The multi-model mean correlation is 0.98, significant at the 99% confidence level. Normalizing the above PM_{2.5} responses by the global mean warming yields rates for the increase in fine particulate matter at $0.17 \pm 0.07 \text{ } \mu\text{g m}^{-3} \text{ K}^{-1}$ ($2.9 \pm 1.1\%$ K $^{-1}$) for the global mean and $0.22 \pm 0.13 \text{ } \mu\text{g m}^{-3} \text{ K}^{-1}$ ($3.7 \pm 1.7\%$ K $^{-1}$) over global land.

As further evidence to support a linear PM_{2.5} increase with global mean temperature, the abrupt-4xCO₂ experiments—where the atmospheric CO₂ concentration is immediately quadrupled—yield a very similar rate for the PM_{2.5} increase (Supplementary Figure 2). Here, we use the same 13 models over years 100-140 of the simulation (global annual mean warming is 5.3 ± 0.6 K). The corresponding global mean PM_{2.5} increase is $0.15 \pm 0.07 \text{ } \mu\text{g m}^{-3} \text{ K}^{-1}$ ($2.6 \pm 1.1\%$ K $^{-1}$); over global land, the increase is $0.20 \pm 0.13 \text{ } \mu\text{g m}^{-3} \text{ K}^{-1}$ ($3.3 \pm 1.7\%$ K $^{-1}$). Moreover, the abrupt-4xCO₂ experiments yield similar conclusions to those presented in the main text based on the 1% per year CO₂ experiments. This implies that the PM_{2.5} response is independent of the warming pathway.

Supplementary Note 2: Additional Details on the Sea Salt Response

Although the increase in SS PM_{2.5} is the third most important contributor to the increase in

$\text{PM}_{2.5}$ over global land, the increase in SS $\text{PM}_{2.5}$ becomes more important when considering the global mean increase in $\text{PM}_{2.5}$ (Supplementary Figure 4). Here, the change in SS $\text{PM}_{2.5}$ contributes 47.6% to the total $\text{PM}_{2.5}$ increase, followed by OA and DU $\text{PM}_{2.5}$ at 34.6 and 14.4%, respectively (sulfate and black carbon contribute 3.4 and <1%, respectively). Most of the SS $\text{PM}_{2.5}$ increase is related to an increase in sea salt emissions ($1.5 \pm 1.3 \text{ kg km}^{-2} \text{ day}^{-1}$ over the global ocean; Supplementary Figure 4), particularly at high latitudes, from increased surface winds and melting of sea ice (Allen et al., 2016; Turnock et al., 2020; Thornhill et al., 2021). For example, the spatial correlation coefficient (over the global ocean) between the multi-model mean change in sea salt emissions and surface wind speed is 0.86; the corresponding correlation between SS $\text{PM}_{2.5}$ and surface wind speed is 0.84 (both significant at the 99% confidence level).

Supplementary Note 3: Wet Removal Efficiency

Outside of emissions, the other important processes controlling the amount of aerosol include removal processes. As mentioned earlier, it is difficult to assess the impact of precipitation changes on wet deposition because of potential changes in precipitation frequency or partitioning between large-scale and convective precipitation. Wet (and dry) removal by themselves are also impacted by the amount of aerosol in the column that is available to be removed. Thus, we analyze the removal efficiencies (e.g., wet removal divided by burden) and precipitation statistics based on models that archived all of the necessary data.

Supplementary Figure 8 shows the response and the model agreement on the sign of the response for dust load, dust wet removal efficiency (wet removal divided by load), dust dry removal efficiency (dry removal divided by load), precipitation, large-scale precipitation

(precipitation minus convective precipitation) and frequency of wet days (% of days with 1 mm day⁻¹ or more of precipitation). Supplementary Figure 8a shows a multi-model mean annual mean increase in dust load in most world regions (particularly over the Sahara and downwind, over the subtropical North Atlantic Ocean), which is robust across the six models (Supplementary Figure 8g). The spatial pattern of the increase in dust load is very similar to that based on DU PM_{2.5} (e.g., Supplementary Figure 3c); the spatial correlation of the responses is 0.90, significant at the 99% confidence level.

Supplementary Figure 8b,c shows a multi-model mean decrease in dust wet and dry removal efficiency throughout most of the tropics (outside of the tropical Pacific) and subtropics, including much of the African continent, which is dominated by a decrease in wet removal efficiency. This includes the Mediterranean region and parts of northern Africa, and most of the subtropical North Atlantic Ocean (i.e., off the coast of west Africa). Supplementary Figure 8h shows that the decrease in wet removal efficiency in these regions is a robust response. The (global) spatial correlation between the dust load response and the wet (dry) removal efficiency response is -0.25 (0.03), the former significant at the 99% confidence level. This suggests an increase in dust load is associated with a decrease in wet removal efficiency (and vice versa). Supplementary Figure 8d,e,f show the multi-model mean precipitation, large-scale precipitation and wet day frequency response. All three show decreases in parts of the subtropics, including the aforementioned Mediterranean region and the subtropical North Atlantic Ocean. Wet day frequency, however, shows more vast decreases that also extend to the mid-latitudes, especially over the oceans. Supplementary Figure 8f shows that this decrease in wet day frequency is robust across the six models, particularly over the north Atlantic Ocean and Mediterranean region/northern Africa, as well as over southern

Africa and most of the Southern Hemisphere mid-latitude ocean. The (global) spatial correlation between the wet removal efficiency response and the precipitation response is 0.49; this improves to 0.63 for large-scale precipitation and 0.68 for wet day frequency (all three are significant at the 99% confidence level).

Thus, this analysis shows that a decrease in wet removal efficiency is also important for the increase in dust; in turn, the decrease in wet removal efficiency appears to be largely related to a decrease in wet day frequency. Such a decrease in the frequency of precipitation promotes an increase in dust lifetime, resulting in a larger burden of dust.

We extend this analysis to BC, OA and SO₄ and find very similar results, with the strongest spatial correlations for SO₄ (Supplementary Figure 9; based on five models). For example, the (global) spatial correlation between the SO₄ load response and the wet (dry) removal efficiency response is -0.47 (-0.12). The (global) spatial correlation between the SO₄ wet removal efficiency response and the precipitation response is 0.59; this improves to 0.68 for large-scale precipitation and 0.82 for wet day frequency. Analysis of SO₄ chemical production (aqueous phase plus gas phase production) shows a lack of robust changes across six models (now shown). This implies that the robust increase in SO₄ (e.g., Supplementary Figure 3g,h; Supplementary Figure 9a,g for SO₄ load) is not due to a robust increase in SO₄ chemical production. This further supports the importance of decreased wet removal efficiency for the robust increase in SO₄.

For OA (based on two models that happen to be NOBVOC models, including CNRM-ESM2-1 and MIROC6), the (global) spatial correlation between the OA load response and the wet (dry) removal efficiency response is -0.15 (-0.24). The (global) spatial correlation between the OA wet removal efficiency response and the precipitation response is 0.40; this

improves to 0.48 for large-scale precipitation and 0.50 for wet day frequency. For BC (based on one model only, CNRM-ESM2-1), the (global) spatial correlation between the BC load response and the wet (dry) removal efficiency response is -0.18 (-0.17). The (global) spatial correlation between the BC wet removal efficiency response and the precipitation response is 0.28; this improves to 0.39 for large-scale precipitation and 0.45 for wet day frequency.

Thus, although we find that an increase in emissions (dust and BVOCs) is the leading cause for the increase in aerosol/PM_{2.5} under increasing atmospheric CO₂ concentrations in CMIP6 models, a decrease in wet removal efficiency also appears to contribute. A targeted analysis devoted to aerosol removal and the associated processes is necessary to further understand the role of removal efficiencies (both wet and dry), as well as the possible importance of other factors.

Supplementary Note 4: UKESM1-0-LL Saharan Dust Response

UKESM1-0-LL includes interactive vegetation effects on dust emissions and it also yields an anomalous nAF dust response; i.e., it is one of three models that yield a decrease in nAF dust emissions, while also yielding the largest decrease in nAF dust emissions (Fig. 4). We further investigate the possible impacts of vegetation changes (via the bare soil fraction) on dust emissions in this model. Although there is a (small) decrease in nAF bare soil fraction at -2.7% (consistent with UKESM1-0-LL's decrease in dust emissions), the spatial correlation between the change in nAF dust emissions and bare soil fraction is 0.47 and 0.13 for the annual and summertime mean. The corresponding correlations between nAF dust emissions and surface wind speed (which decreases in UKESM1-0-LL, unlike most models) are larger at 0.50 and 0.80, respectively. Thus, changes in vegetation may contribute to the Saharan

dust response in this model under 1% per year CO₂, but surface winds remain the likely driver, particularly during summertime (JAS).

Supplementary Note 5: GISS-E2-1-G OMA versus MATRIX

We use the One-Moment Aerosol (OMA) version of the GISS-E2-1-G model (physics version 3), as the Multiconfiguration Aerosol TRacker of mIXing state (MATRIX) (Bauer et al., 2020) version (physics version 5) does not include interactive SOA production. MATRIX has the SOA-yield approach for SOA (not the partitioning that allows for SOA evaporation in OMA), but only uses prescribed terpenes (which do not respond to climate) as SOA precursors. However, similar results are obtained with both versions of the GISS-E2-1-G model (but for different reasons, particularly in the context of OA PM_{2.5}). For example, the global land PM_{2.5} increase under 1% per year CO₂ is 0.29 and 0.25 $\mu\text{g m}^{-3}$ in OMA and MATRIX, respectively. The somewhat larger PM_{2.5} increase in OMA is due to a larger DU PM_{2.5} increase over global land, at 0.22 $\mu\text{g m}^{-3}$ (compared to 0.16 $\mu\text{g m}^{-3}$ in MATRIX). The global land OA PM_{2.5} increase is relatively small in both models (\sim 1%) at 0.01 and 0.02 $\mu\text{g m}^{-3}$ in OMA and MATRIX, respectively. The relatively small OA PM_{2.5} response in MATRIX is due to the above reasons (i.e., uses prescribed terpenes as SOA precursors, which do not respond to climate). The relatively small OA PM_{2.5} response in OMA is due to the responses discussed in the main text (i.e., includes gas-particle partitioning of semi-volatile species, which limits SOA formation from the oxidation of BVOCs).

Supplementary Note 6: Isoprene Emission Responses

GISS-E2-1-G, NorESM2-LM and GFDL-ESM4 yield increases in global land isoprene emis-

sions 50%, 61% and 83% as large as the increase in BVOC emissions, respectively, under 1% per year CO₂ (Supplementary Figure 13). Thus, the total BVOC emissions increase is largely due to increased isoprene emissions, particularly for GFDL-ESM4. Furthermore, these models yield similar correlations between surface warming and isoprene emissions, as between surface warming and BVOC emissions, under 1% per year CO₂. UKESM1-0-LL, however, shows a negligible increase in isoprene emissions (0.41 kg km⁻² day⁻¹; 3.2%) under 1% per year CO₂ (13% of the increase in BVOCs), which is largely due to a decrease in isoprene emissions in 1% per year CO₂-bgc (-4.5 kg km⁻² day⁻¹; -35.3%). As the 1% per year CO₂-bgc experiment isolates the impact of CO₂ on biogeochemical processes, this result clearly shows the importance of inhibited isoprene emissions under increasing CO₂ concentrations in UKESM1-0-LL (Pacifico et al., 2012; Arneth et al., 2007), which accounts for this model's weaker increase in BVOC emissions.

We note that these responses are not additive; that is, the sum of the change in the BVOC or isoprene emissions in the radiatively coupled and biogeochemcially coupled experiments does not equal the corresponding change in the fully coupled 1% per year CO₂ experiment. Thus, non-linear feedbacks between radiative and biogeochemical processes impact BVOC emissions, and in turn, SOA. It should also be noted that NorESM2-LM, GFDL-ESM4, and CESM2-WACCM utilize the Model of Emissions of Gases and Aerosols from Nature (MEGAN, Guenther et al., 2012), which may in part explain the similarity of the results in these three models.

Supplementary Note 7: Archived versus Approximated PM_{2.5}

Six models archived PM_{2.5}, including GFDL-ESM4, GISS-E2-1-G, MIROC-ES2L, MIROC6,

MPI-ESM1-2-HAM and MRI-ESM2-0. Comparing the climatology of archived PM_{2.5} with our approximate PM_{2.5} further shows that the approximate PM_{2.5} provides a conservative estimate of fine particulate air pollution. For example, the multi-model annual global mean PM_{2.5} climatology is 7.5 and 4.6 $\mu\text{g m}^{-3}$ based on archived versus approximate PM_{2.5}. Most of the underestimation in the approximated PM_{2.5} is related to underestimation of fine dust. This is supported through visual interpretation (Supplementary Figure 15), as well as prior and more comprehensive analyses (Zhao et al., 2021), and other lines of evidence. For example, the underestimation increases over land (a dust source), where the global mean climatological PM_{2.5} is 10.3 versus 5.1 $\mu\text{g m}^{-3}$ based on archived versus approximate PM_{2.5}. The underestimation is not due to lack of species (e.g., nitrate) in the approximate PM_{2.5}. The global mean climatology of nitrate and ammonium aerosol averaged over the two models that include it (GFDL-ESM4, GISS-E2-1-G) is relatively small at 0.01 and 0.06 $\mu\text{g m}^{-3}$, respectively (0.02 and 0.06 $\mu\text{g m}^{-3}$ for global land).

Comparing the response (years 100-140 in the 1% per year CO₂ experiment versus the preindustrial control experiment) of archived versus approximated PM_{2.5} (Supplementary Figure 15) also shows that the approximate PM_{2.5} response to CO₂ increases provides a conservative estimate. For example, the global annual multi-model mean change (in the six models above) is 0.69 versus 0.45 $\mu\text{g m}^{-3}$ based on archived versus approximate PM_{2.5}. Over global land, the corresponding values are 0.90 versus 0.61 $\mu\text{g m}^{-3}$. Changes in nitrate and ammonium contribute only a small amount to the total PM_{2.5} response (and yield conflicting results across the two models). For example, the global mean change in nitrate is $-0.002 \mu\text{g m}^{-3}$ (-46.4%) and $0.003 \mu\text{g m}^{-3}$ (17.9%) in GFDL-ESM4 and GISS-E2-1-G, respectively. The corresponding responses for ammonium are $-0.011 \mu\text{g m}^{-3}$ (-20.6%) and $0.001 \mu\text{g m}^{-3}$

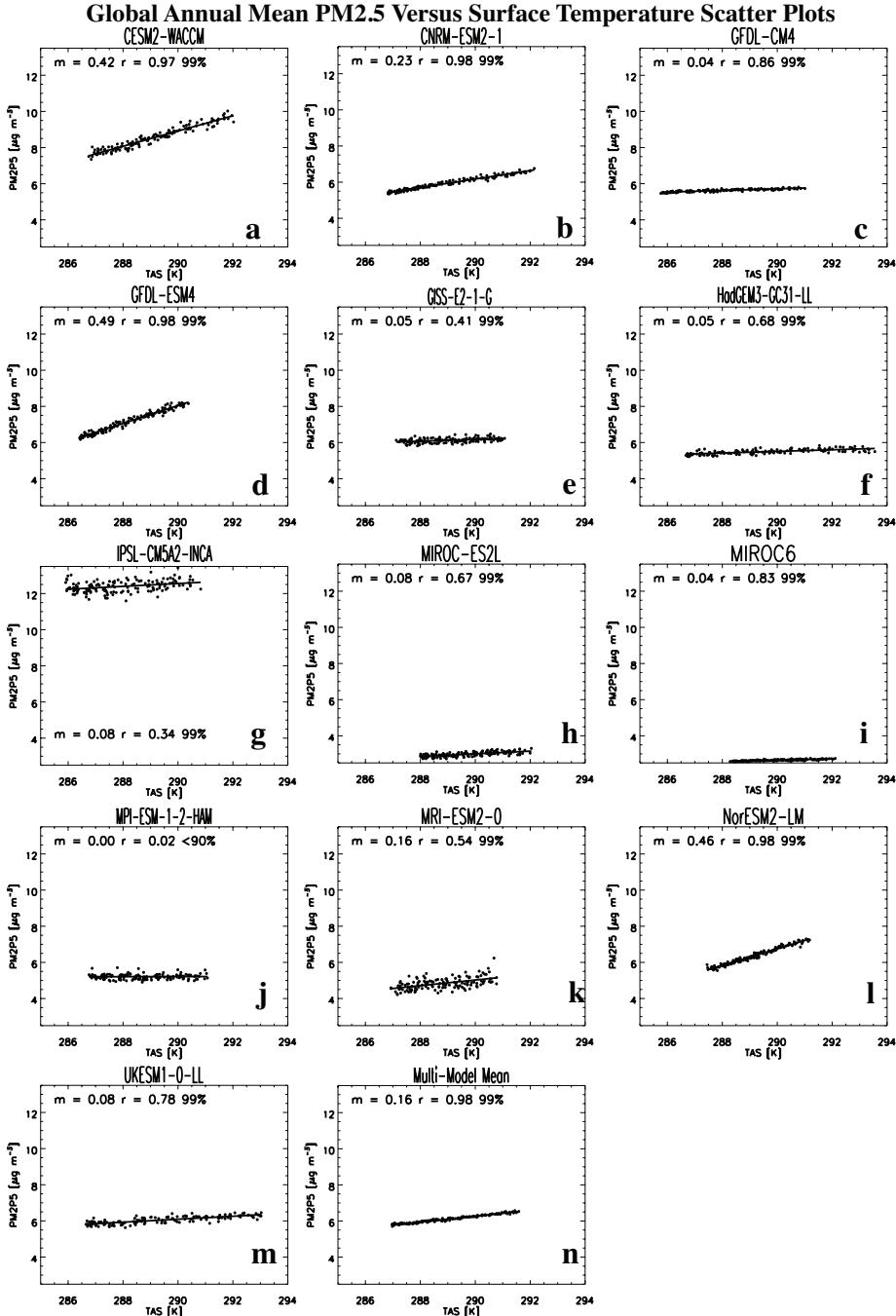
(2.3%) for GFDL-ESM4 and GISS-E2-1-G, respectively. Thus, our quoted PM_{2.5} responses are also conservative, and relative to archived PM_{2.5}, about 1/3 lower. In terms of percent changes, however, the approximated PM_{2.5} yields somewhat higher values (due to the smaller climatological PM_{2.5}). The global mean PM_{2.5} percent change is 9.2% versus 9.9% based on archived versus approximated PM_{2.5}. Over global land, the corresponding percent changes are 8.7% versus 12.0%.

Supplementary Note 8: Alternative PM_{2.5} Approximation (0.3 DU Factor)

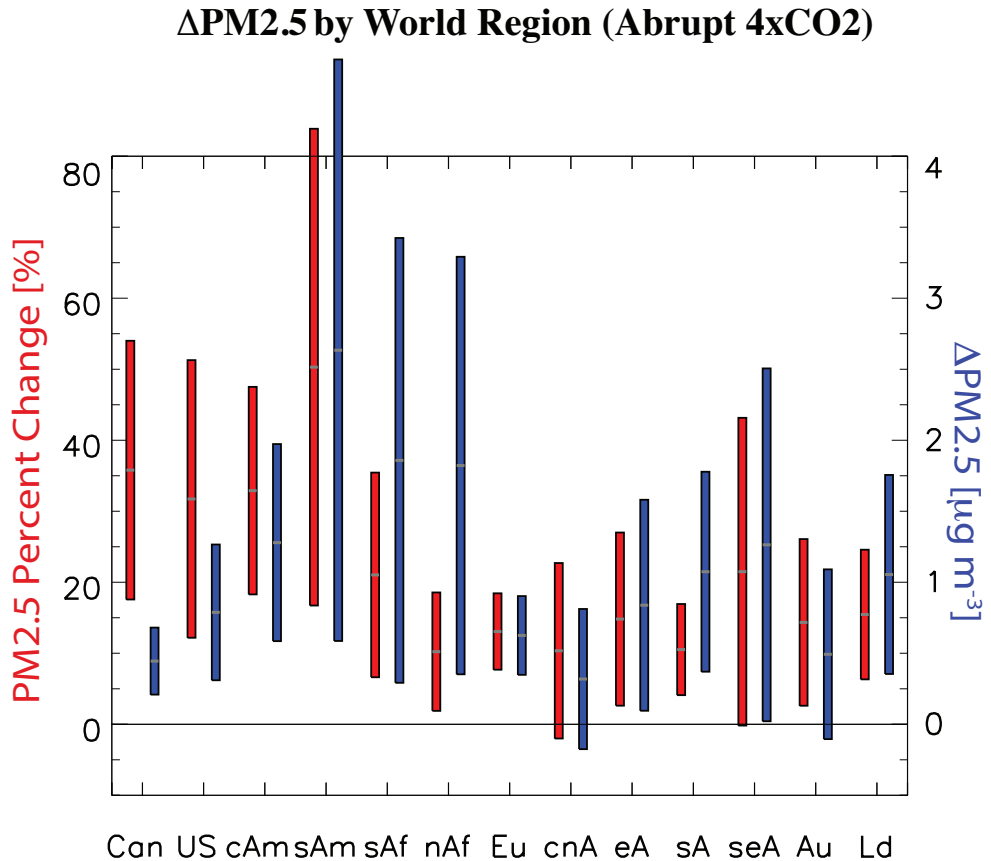
If we adopt a fine dust scaling factor of 0.3 (as opposed to 0.1), which was previously derived from MERRA-2 (Zhao et al., 2021), we obtain similar conclusions, but with larger absolute increases in DU PM_{2.5} and in turn, PM_{2.5} (Supplementary Figure 16). For example, the global multi-model mean PM_{2.5} increase is $0.80 \pm 0.37 \mu\text{g m}^{-3}$ ($9.7 \pm 4.1\%$). This is about 30% larger than the original increase (using a fine dust factor of 0.1) of $0.62 \pm 0.26 \mu\text{g m}^{-3}$ ($10.8 \pm 3.9\%$). Twelve of thirteen models yield an increase, ranging from $-0.52 \mu\text{g m}^{-3}$ in MPI-ESM1-2-HAM to $2.4 \mu\text{g m}^{-3}$ in GFDL-ESM4. Over global land, the multi-model mean increase is $1.3 \pm 0.8 \mu\text{g m}^{-3}$ ($10.0 \pm 5.7\%$). This is about 57% larger than the original increase of $0.83 \pm 0.49 \mu\text{g m}^{-3}$ ($13.7 \pm 6.3\%$). Eleven of thirteen models yield an increase, ranging from $-1.8 \mu\text{g m}^{-3}$ in MPI-ESM1-2-HAM (and $-0.44 \mu\text{g m}^{-3}$ in UKESM1-0-LL) to $4.3 \mu\text{g m}^{-3}$ in GFDL-ESM4. As expected, the change in DU PM_{2.5} now contributes more to the total PM_{2.5} increase at 52.3%, followed by OA PM_{2.5} at 41.5%. The original contributions were 26.8% and 63.7% for DU and OA PM_{2.5}, respectively.

Supplementary Note 9: Fire Responses to Increasing CO₂ and Warming

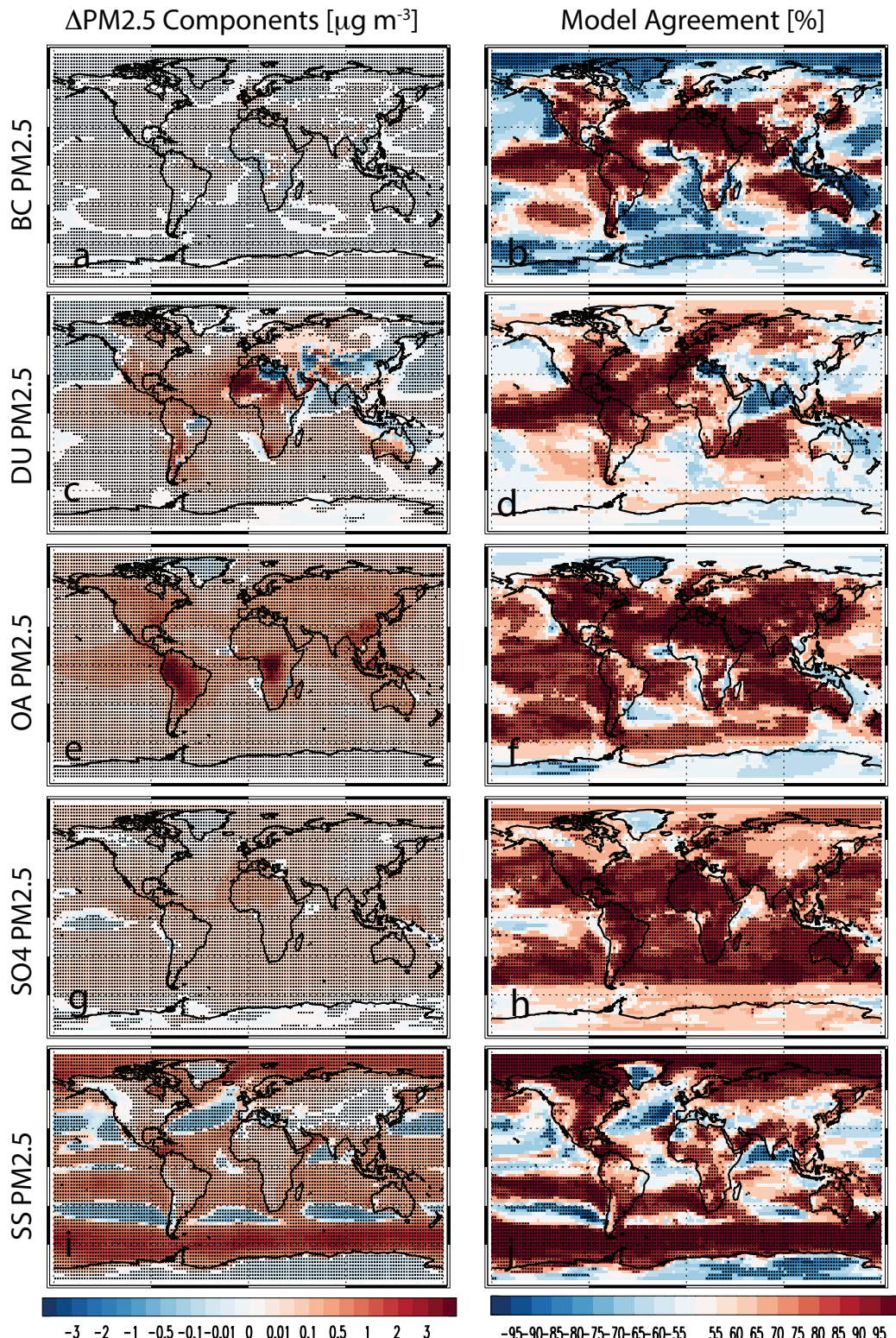
Another reason why our quoted PM_{2.5} responses are conservative is due to the lack of climate-change induced PM_{2.5} from natural fires. Five models include interactive fire modules (e.g., Rabin et al., 2017) coupled to their dynamic vegetation and archived the relevant data, including MPI-ESM-1-2-HAM, CESM2-WACCM, CNRM-ESM2-1, MRI-ESM2-0 and NorESM2-LM. Although these models do not directly calculate the resulting changes in PM_{2.5} from fires, all five yield an increase in global land CO₂ emissions from (natural) fires (“fFire”) under 1% per year CO₂ (Supplementary Figure 14). The multi-model mean increase is $26.22 \pm 8.7 \text{ kgC km}^{-2} \text{ day}^{-1}$ ($72.4 \pm 24.2\%$), ranging from 39.9% to 127.5% in CNRM-ESM2-1 and MPI-ESM-1-2-HAM, respectively, and all world regions experience an increase under the multi-model mean. This implies an increase in PM_{2.5} (i.e., carbonaceous aerosols) from natural fires under increasing CO₂ (which we do not account for here). Three of these five models also conducted the 1% per year CO₂-rad and 1% per year CO₂-bgc simulations and archived the relevant data. The increase in CO₂ emissions from fires is largely due to CO₂ effects on vegetation (as opposed to the radiative effects). Under 1% per year CO₂-bgc simulations, CNRM-ESM2-1, MRI-ESM2-0 and NorESM2-LM yield increases in CO₂ emissions from fires of 49.4, 108.8 and 26.4%, respectively. The corresponding responses under 1% per year CO₂-rad simulations are -29.1 , -22.9 and 17.5% .



SUPPLEMENTARY FIGURE 1 Global mean annual mean PM_{2.5} versus surface temperature for each model in years 1-140 from 1% per year CO₂ experiments. PM_{2.5} [$\mu\text{g m}^{-3}$] versus TAS [K] for (a) CESM2-WACCM; (b) CNRM-ESM2-1; (c) GFDL-CM4; (d) GFDL-ESM4; (e) GISS-E2-1-G; (f) HadGEM3-GC31-LL; (g) IPSL-CM5A2-INCA; (h) MIROC-ES2L; (i) MIROC6; (j) MPI-ESM-1-2-HAM; (k) MRI-ESM2-0; (l) NorESM2-LM; (m) UKESM1-0-LL; and (n) the multi-model mean. Also included is the least-squares regression slope (m; units of [$\mu\text{g m}^{-3} \text{ K}^{-1}$]), correlation coefficient (r) and its significance level. Much of the model diversity in climatological PM_{2.5} is due to SS PM_{2.5}. For example, IPSL-CM5A2-INCA has the largest climatological PM_{2.5}, and it also has the largest climatological SS PM_{2.5} (at 11.0 $\mu\text{g m}^{-3}$, relative to the multi-model mean of 3.5 $\mu\text{g m}^{-3}$). Similarly, MIROC6, MIROC-ES2L and MRI-ESM2-0 have relatively low climatological PM_{2.5}, as well as SS PM_{2.5}.

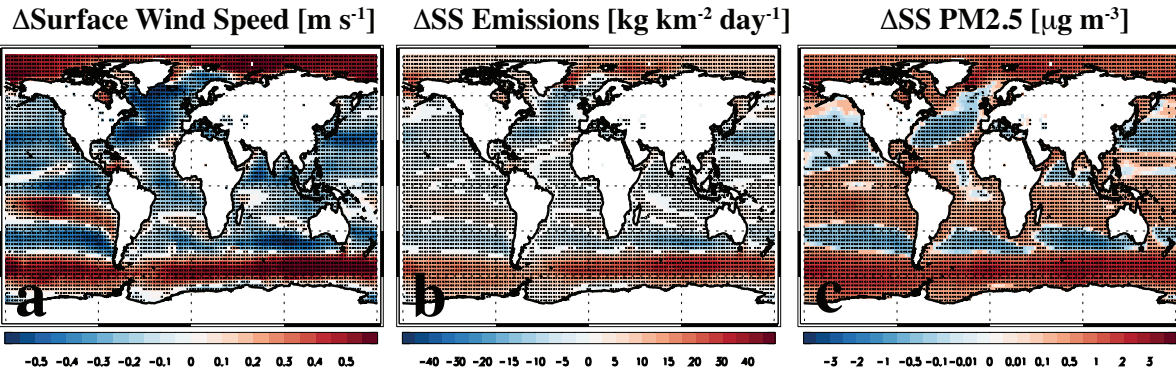


SUPPLEMENTARY FIGURE 2 PM_{2.5} response to GHG-induced warming to abrupt 4xCO₂ experiments. Absolute [$\mu\text{g m}^{-3}$] and relative [%] PM_{2.5} response by world region. Bar center (gray horizontal line) shows the multi-model mean response and bar length represents the 90% confidence interval estimated as $\frac{1.65 \times \sigma}{\sqrt{n_m}}$, where σ is the standard deviation across models and n_m is the number of models. World regions are identical to those in Figure 1. The same 13 models as in the 1% per year CO₂ analysis are used here (over years 100-140 of the abrupt-4xCO₂ simulation relative to the preindustrial control).

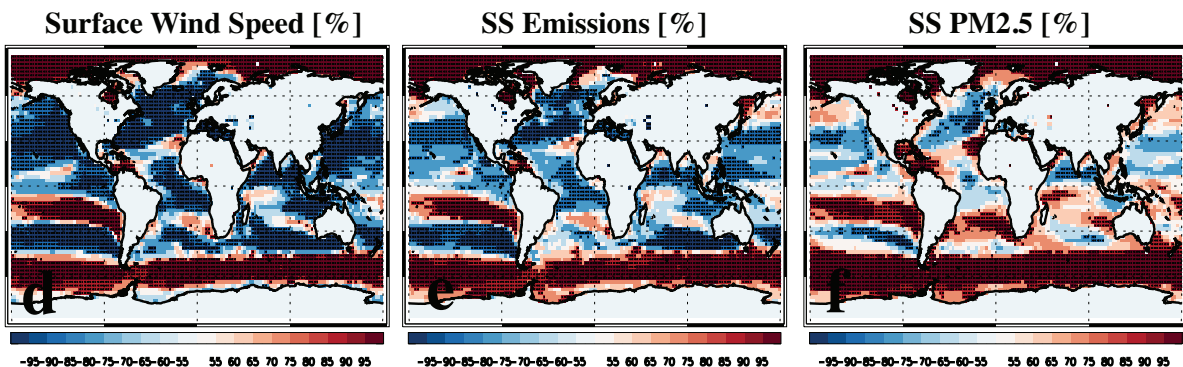


SUPPLEMENTARY FIGURE 3 Annual mean PM_{2.5} components. Multi-model mean annual mean response [$\mu\text{g m}^{-3}$] of (a) BC PM_{2.5}; (c) DU PM_{2.5}; (e) OA PM_{2.5}; (g) SO₄ PM_{2.5}; and (i) SS PM_{2.5}. Dots in panels (a, c, e, g, i) represent a significant response at the 90% confidence level based on a two-tailed pooled *t*-test. Corresponding model agreement [%] on the sign of the response for (b) BC PM_{2.5}; (d) DU PM_{2.5}; (f) OA PM_{2.5}; (h) SO₄ PM_{2.5}; and (j) SS PM_{2.5}. In panels (b, d, f, h, j), red (blue) colors indicate model agreement on an increase (decrease) and dots represent a significant model agreement at the 90% confidence level based on a two-tailed binomial test.

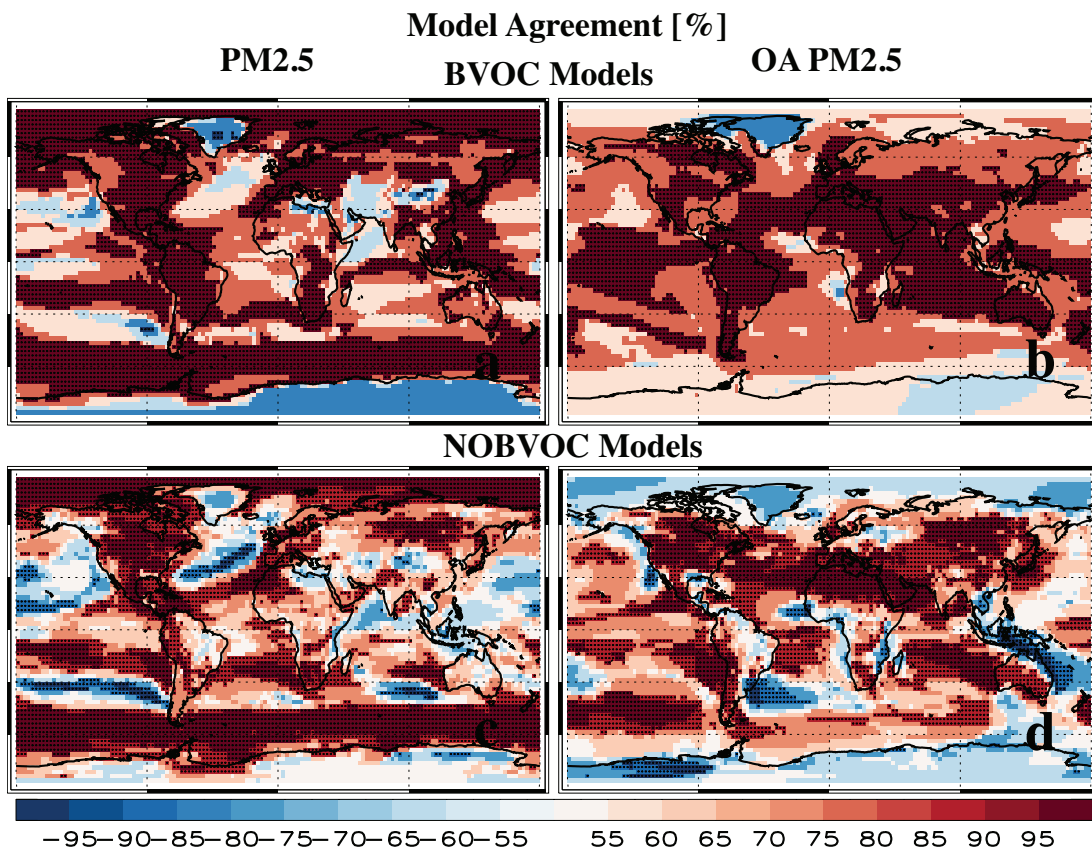
Multi-Model Mean Annual Mean Response



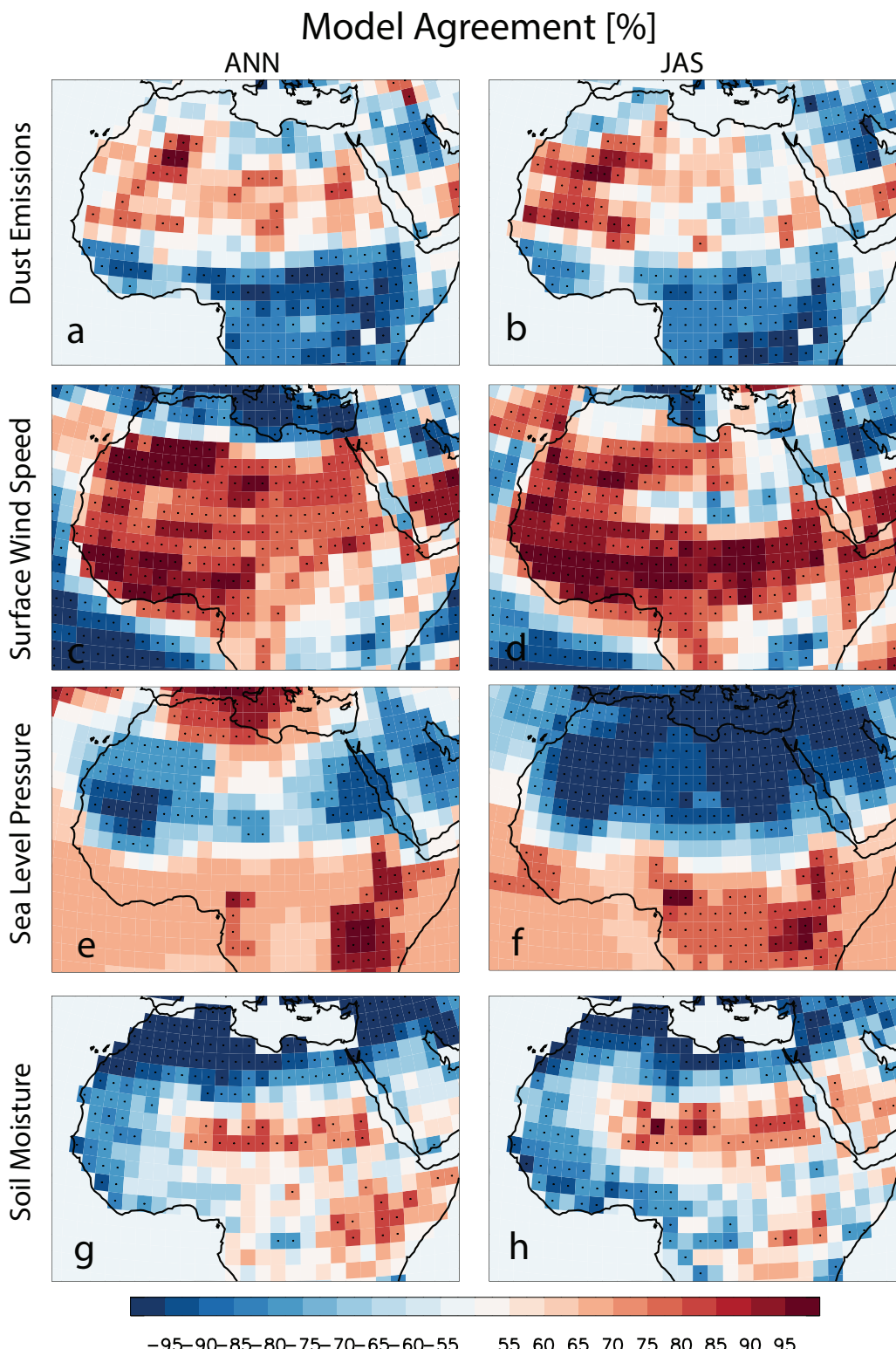
Model Agreement



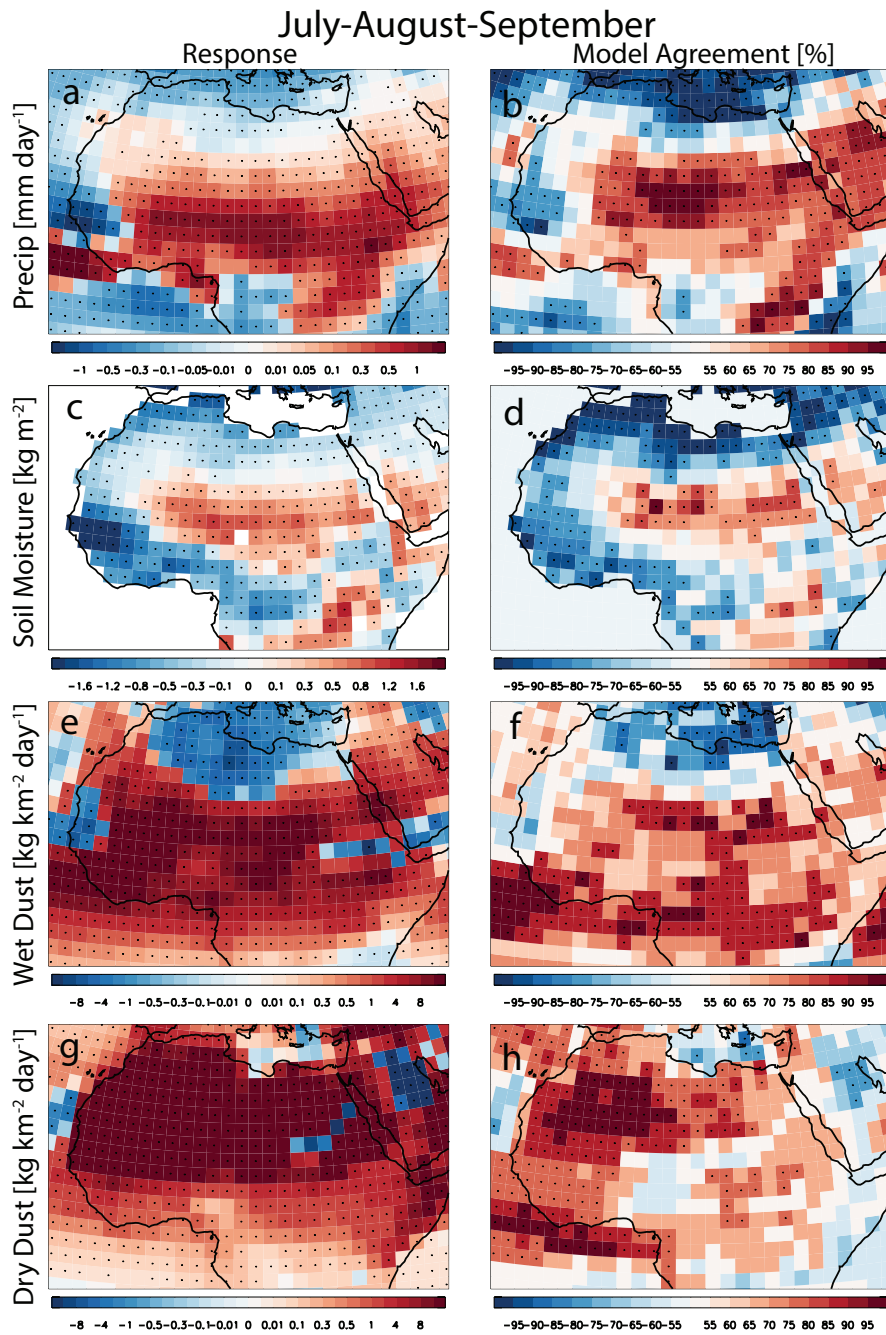
SUPPLEMENTARY FIGURE 4 Sea-salt related responses under GHG-induced warming. Multi-model mean annual mean response of (a) surface wind speed [$m s^{-1}$], (b) sea-salt emissions [$kg km^{-2} day^{-1}$] and (c) SS PM_{2.5} [$\mu g m^{-3}$]. Dots in panels (a, b, c) represent a significant response at the 90% confidence level based on a two-tailed pooled *t*-test. Model agreement [%] on the sign of the annual mean response for (d) surface wind speed, (e) sea-salt emissions, and (f) SS PM_{2.5}. Dots in panels (d, e, f) represent a significant model agreement at the 90% confidence level based on a two-tailed binomial test. Due to limited data availability, this figure is based on 8 models including GFDL-ESM4, GISS-E2-1-G, IPSL-CM5A2-INCA, MIROC-ES2L, MIROC6, MPI-ESM-1-2-HAM, MRI-ESM2-0 and NorESM2-LM. CNRM-ESM2-1 was excluded to avoid biasing the multi-model mean (this model has about 50 times the sea salt emissions as other models).



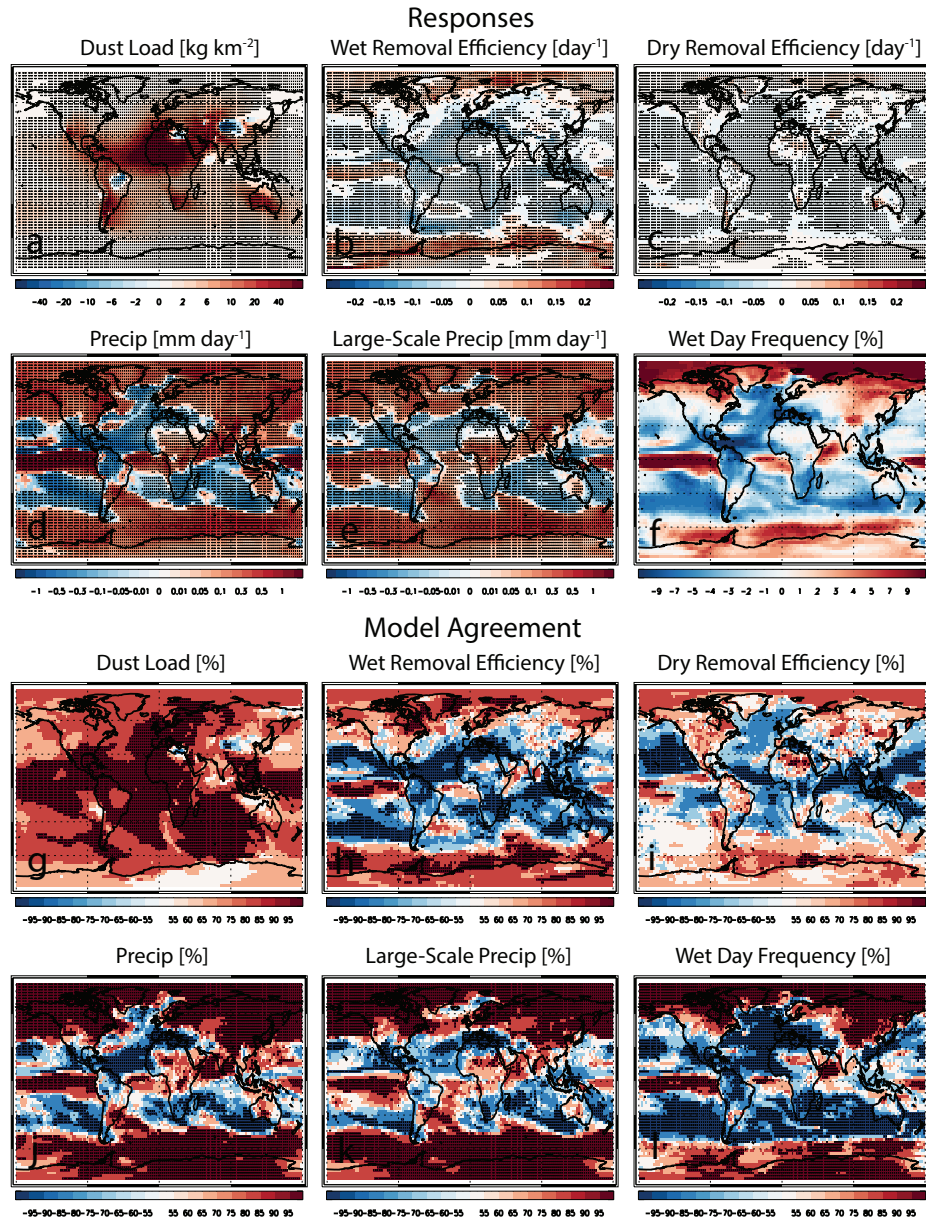
SUPPLEMENTARY FIGURE 5 Model agreement on the sign of the PM_{2.5} and OA PM_{2.5} response to GHG-induced warming in two model subsets. Model agreement [%] on the sign of the annual mean response for (a) PM_{2.5} and (b) OA PM_{2.5} in five models with climate dependent BVOC emissions (BVOC models); and (c, d) the corresponding model agreement in eight models that lack climate dependent BVOC emissions (NOBVOC models). Dots represent a significant model agreement at the 90% confidence level based on a two-tailed binomial test.



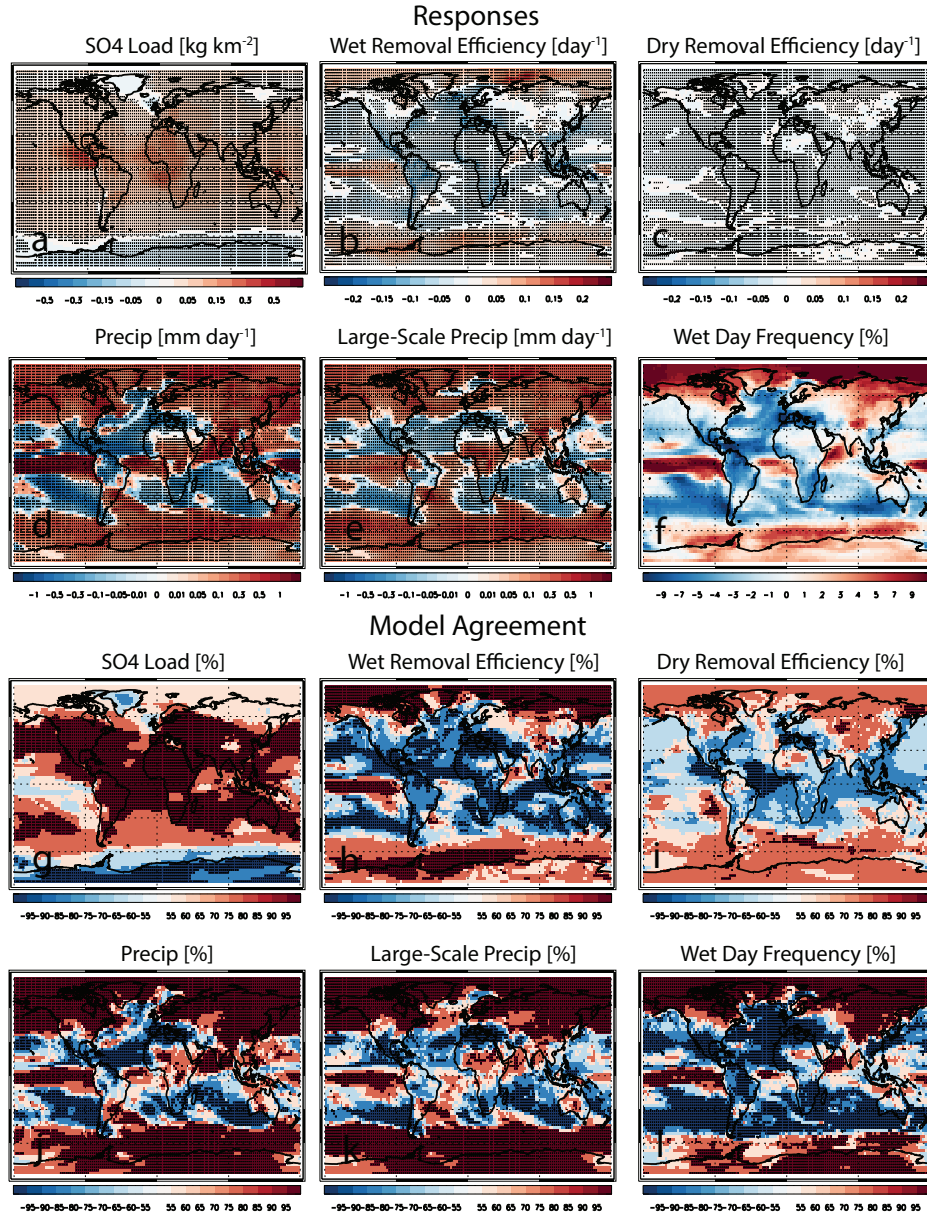
SUPPLEMENTARY FIGURE 6 Model agreement on the sign of the response of dust emissions and atmospheric dynamics to GHG-induced warming over Africa. Model agreement [%] on the sign of the annual mean response for (a) dust emissions; (c) surface wind speed; (e) sea level pressure; and (g) surface soil moisture. Corresponding July-August-September (JAS) model agreement for (b) dust emissions; (d) surface wind speed; (f) sea level pressure; and (h) surface soil moisture. Dots represent a significant model agreement at the 90% confidence level based on a two-tailed binomial test. 100% of models yield warming over the entire region (not included).



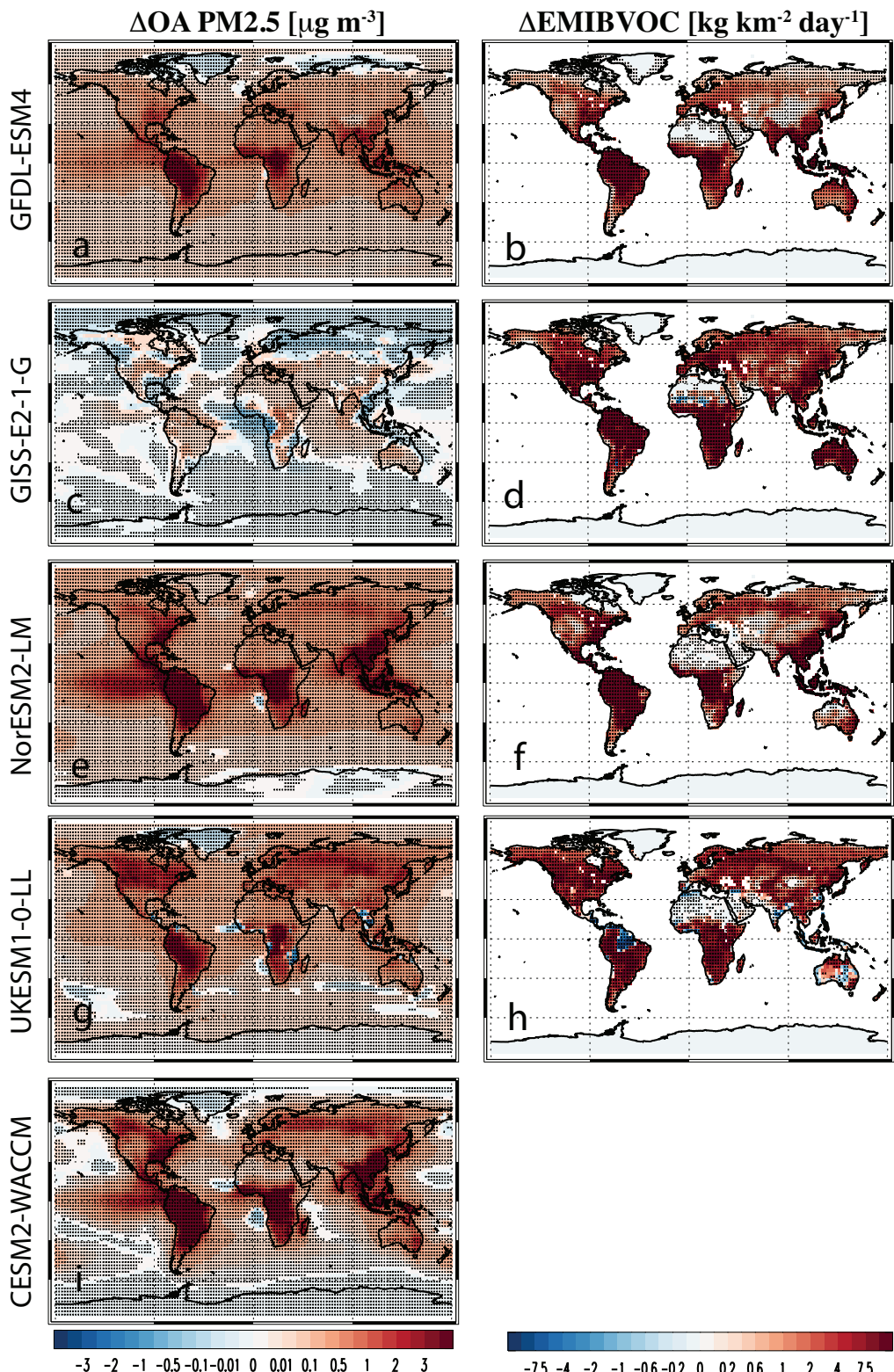
SUPPLEMENTARY FIGURE 7 Additional July-August-September responses to GHG-induced warming over Africa. Multi-model mean JAS mean (a) precipitation [mm day^{-1}]; (c) surface soil moisture [kg m^{-2}]; (e) dust wet deposition [$\text{kg km}^{-2} \text{ day}^{-1}$]; and (g) dust dry deposition [$\text{kg km}^{-2} \text{ day}^{-1}$] responses. Dots in panels (a, c, e, g) represent a significant response at the 90% confidence level based on a two-tailed pooled t -test. Corresponding model agreement [%] on the sign of the JAS response for (b) precipitation; (d) surface soil moisture; (f) dust wet deposition; and (h) dust dry deposition. In panels (b, d, f, h), red (blue) colors indicate model agreement on an increase (decrease) and dots represent a significant model agreement at the 90% confidence level based on a two-tailed binomial test. Due to limited data availability, the surface soil moisture plots (c, d) are based on 12 models (HadGEM3-GC31-LL is missing); the dust wet and dry deposition plots (e, f, g, h) are based on 8 models (NorESM2-LM, UKESM1-0-LL, GFDL-CM4, MPI-ESM-1-2-HAM and HadGEM3-GC31-LL are missing).



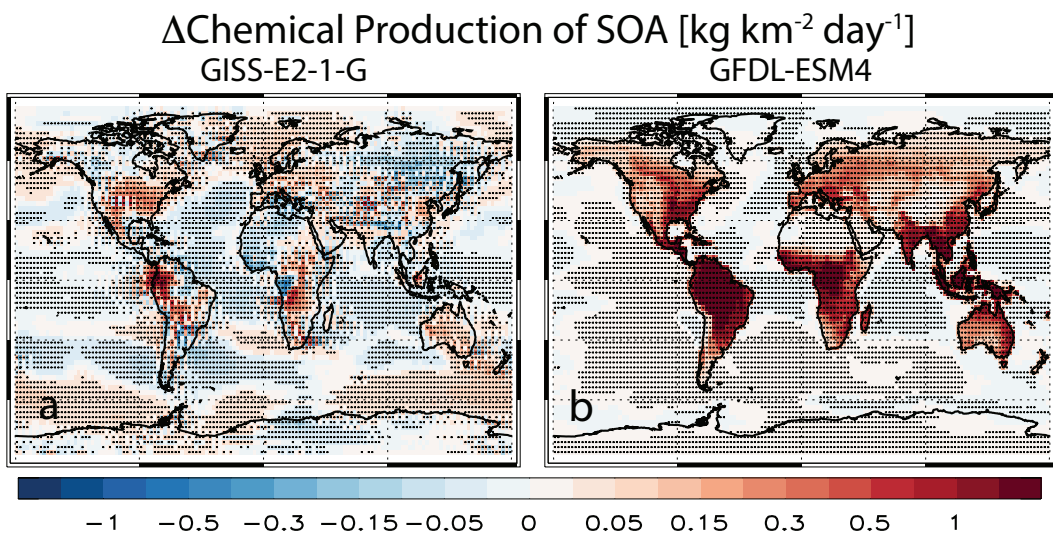
SUPPLEMENTARY FIGURE 8 Dust aerosol removal efficiencies. Multi-model mean ANN mean (a) dust load [kg km^{-2}]; (b) dust wet removal efficiency [day^{-1}]; (c) dust dry removal efficiency [day^{-1}]; (d) precipitation [mm day^{-1}]; (e) large-scale precipitation [mm day^{-1}]; and (f) wet day frequency [%] responses. Dots represent a significant response at the 90% confidence level based on a two-tailed pooled t -test (not included in panel f). Corresponding model agreement [%] on the sign of the ANN response for (g) dust load; (h) dust wet removal efficiency; (i) dust dry removal efficiency; (j) precipitation; (k) large-scale precipitation; and (l) wet day frequency. In panels (g-l), red (blue) colors indicate model agreement on an increase (decrease) and dots represent a significant model agreement at the 90% confidence level based on a two-tailed binomial test. Due to limited data availability, these plots are based on 6 models, including CESM2-WACCM, CNRM-ESM2-1, GFDL-ESM4, MIROC6, MIROC-ES2L and MRI-ESM2-0.



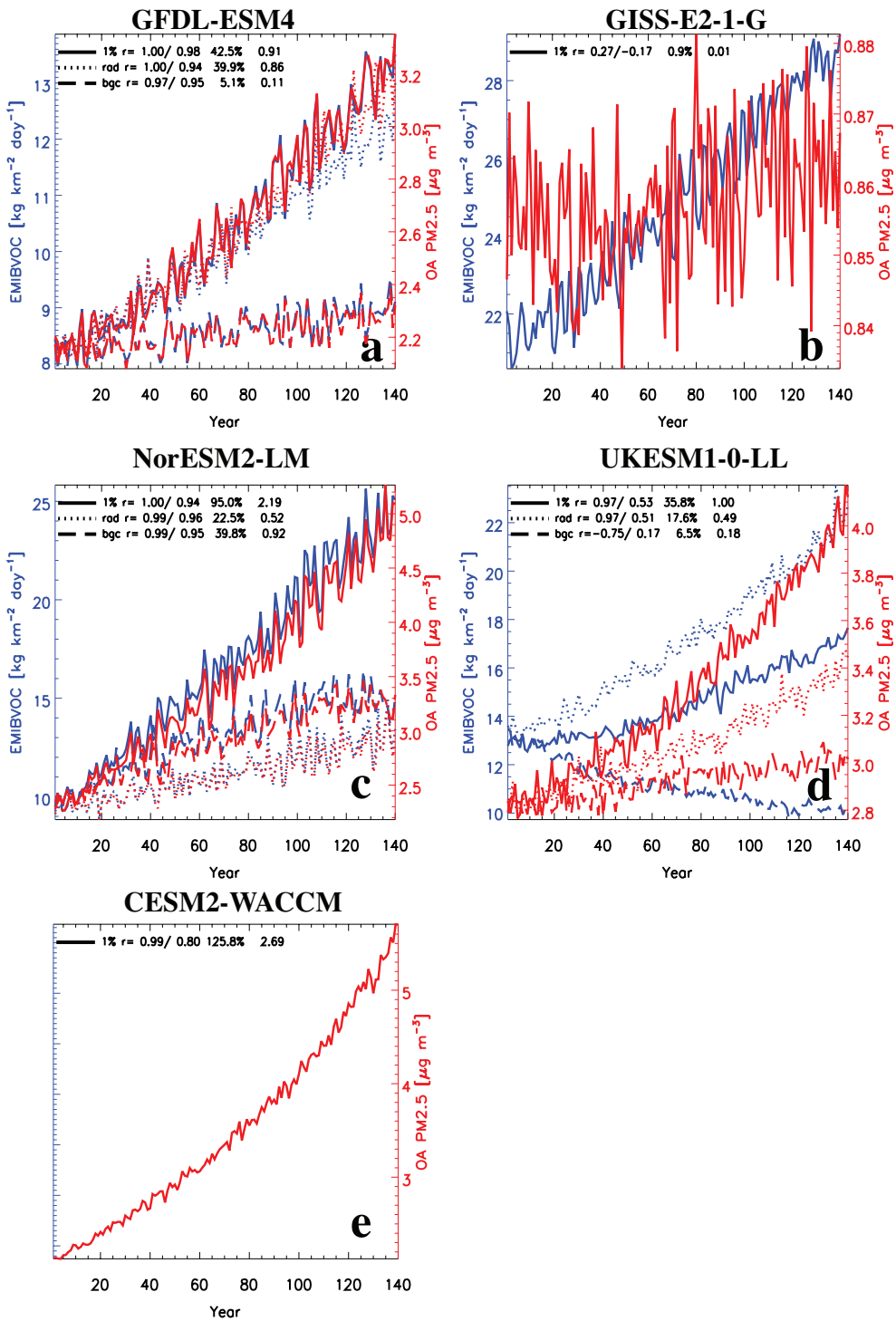
SUPPLEMENTARY FIGURE 9 Sulfate aerosol removal efficiencies. Multi-model mean ANN mean (a) SO₄ load [kg km⁻²]; (b) SO₄ wet removal efficiency [day⁻¹]; (c) SO₄ dry removal efficiency [day⁻¹]; (d) precipitation [mm day⁻¹]; (e) large-scale precipitation [mm day⁻¹]; and (f) wet day frequency [%] responses. Dots represent a significant response at the 90% confidence level based on a two-tailed pooled *t*-test (not included in panel f). Corresponding model agreement [%] on the sign of the ANN response for (g) SO₄ load; (h) SO₄ wet removal efficiency; (i) SO₄ dry removal efficiency; (j) precipitation; (k) large-scale precipitation; and (l) wet day frequency. In panels (g-l), red (blue) colors indicate model agreement on an increase (decrease) and dots represent a significant model agreement at the 90% confidence level based on a two-tailed binomial test. Due to limited data availability, these plots are based on 5 models, including CNRM-ESM2-1, GFDL-ESM4, MIROC6, MIROC-ES2L and MRI-ESM2-0.



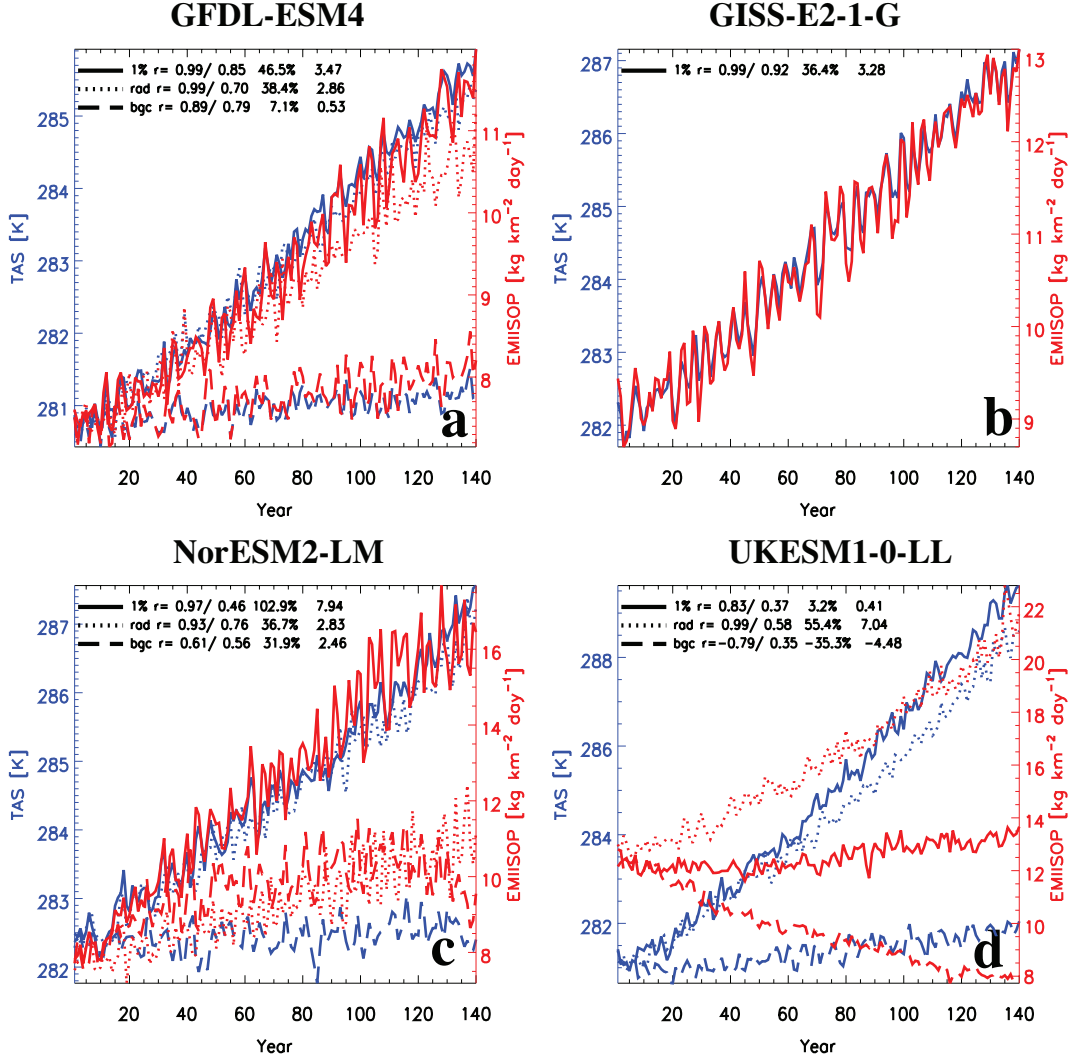
SUPPLEMENTARY FIGURE 10 Annual mean OA PM_{2.5} and BVOC emissions responses to GHG-induced warming in models with climate-dependent BVOC emissions. Annual mean OA PM_{2.5} [$\mu\text{g m}^{-3}$] response in (a) GFDL-ESM4; (c) GISS-E2-1-G; (e) NorESM2-LM; (g) UKESM1-0-LL; and (i) CESM2-WACCM. Corresponding annual mean response of BVOC emissions [$\text{kg km}^{-2} \text{ day}^{-1}$] for (b) GFDL-ESM4; (d) GISS-E2-1-G; (f) NorESM2-LM; and (h) UKESM1-0-LL. CESM2-WACCM lacks BVOC emissions data. Dots represent a significant response at the 90% confidence level based on a two-tailed pooled *t*-test.



SUPPLEMENTARY FIGURE 11 Annual mean chemical SOA production response to GHG-induced warming in two models with climate-dependent BVOC emissions. Annual mean chemical SOA production [$\text{kg km}^{-2} \text{ day}^{-1}$] response in (a) GISS-E2-1-G and (b) GFDL-ESM4. Other BVOC models lack data. Dots represent a significant response at the 90% confidence level based on a two-tailed t -test.

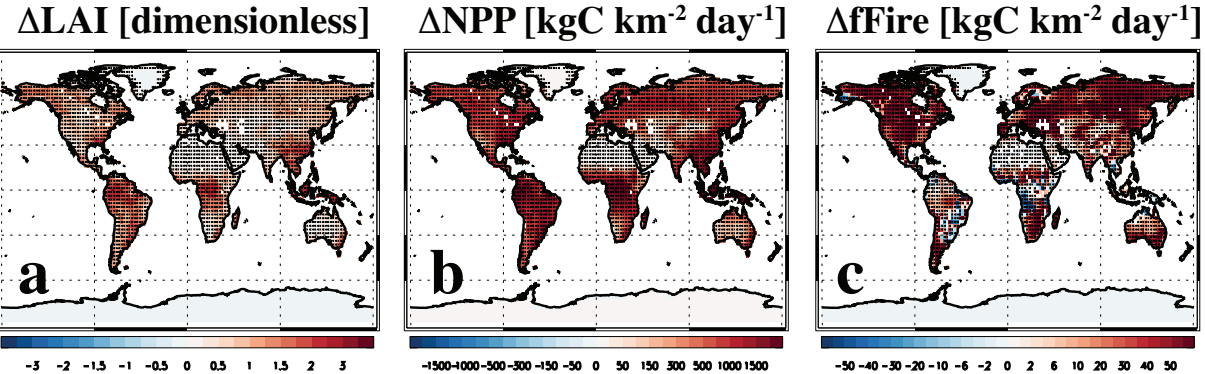


SUPPLEMENTARY FIGURE 12 **Global land mean time series of BVOC emissions and OA PM_{2.5}.** BVOC emissions (EMIBVOC; blue) [$\text{kg km}^{-2} \text{ day}^{-1}$] and OA PM_{2.5} (red) [$\mu\text{g m}^{-3}$] for five models that include climate dependent BVOC emissions, including (a) GFDL-ESM4; (b) GISS-E2-1-G; (c) NorESM2-LM; (d) UKESM1-0-LL; and (e) CESM2-WACCM (which lacks EMIBVOC data). Solid, dotted and dashed lines show results from the 1% per year CO₂, 1% per year CO₂-rad, and 1% per year CO₂-bgc experiments (only three models, GFDL-ESM4, NorESM2-LM and UKESM1-0-LL, performed the latter two experiments). Also included is the correlation coefficient (r), followed by the detrended correlation, the percent change and the absolute change in isoprene emissions (years 100-140 relative to 40 years from the preindustrial control).

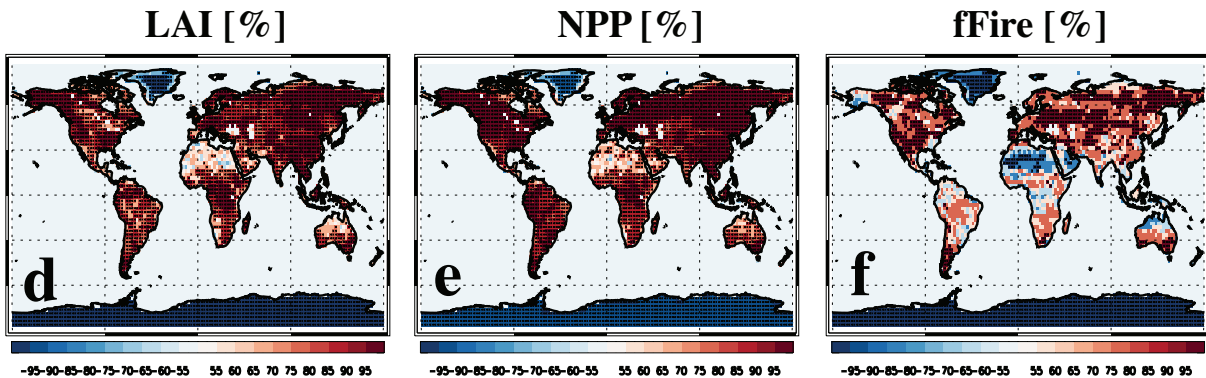


SUPPLEMENTARY FIGURE 13 Global land mean time series of surface temperature and isoprene emissions. Surface temperature (TAS; blue) [K] and isoprene emissions (EMIISOP; red) [$\text{kg km}^{-2} \text{ day}^{-1}$] for four models that include climate dependent isoprene emissions, including (a) GFDL-ESM4; (b) GISS-E2-1-G; (c) NorESM2-LM; and (d) UKESM1-0-LL. Solid, dotted and dashed lines show results from the 1% per year CO_2 , 1% per year CO_2 -rad, and 1% per year CO_2 -bgc experiments (only three models, GFDL-ESM4, NorESM2-LM and UKESM1-0-LL, performed the latter two experiments). Also included is the correlation coefficient (r), followed by the detrended correlation, the percent change and the absolute change in isoprene emissions (years 100-140 relative to 40 years from the preindustrial control).

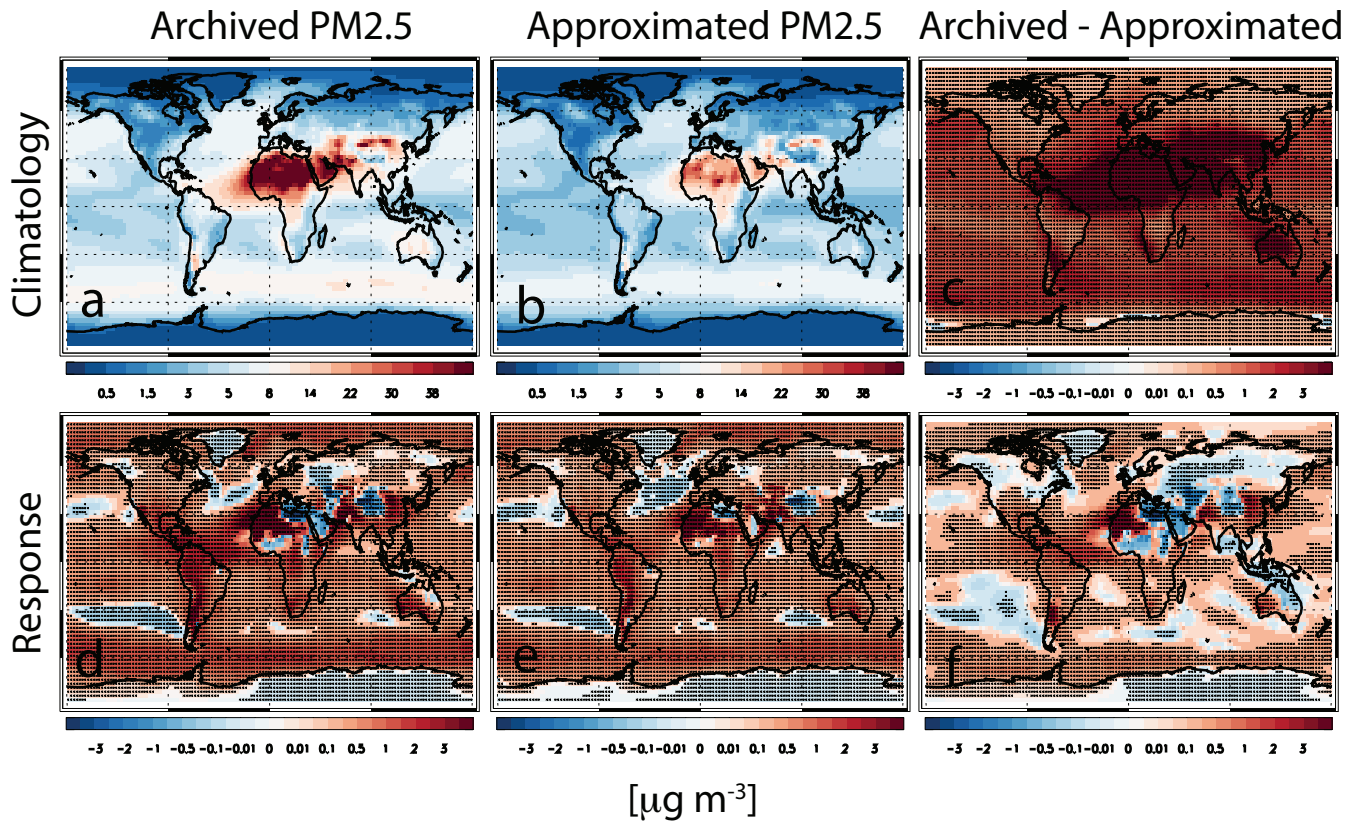
Multi-Model Mean Annual Mean Response



Model Agreement

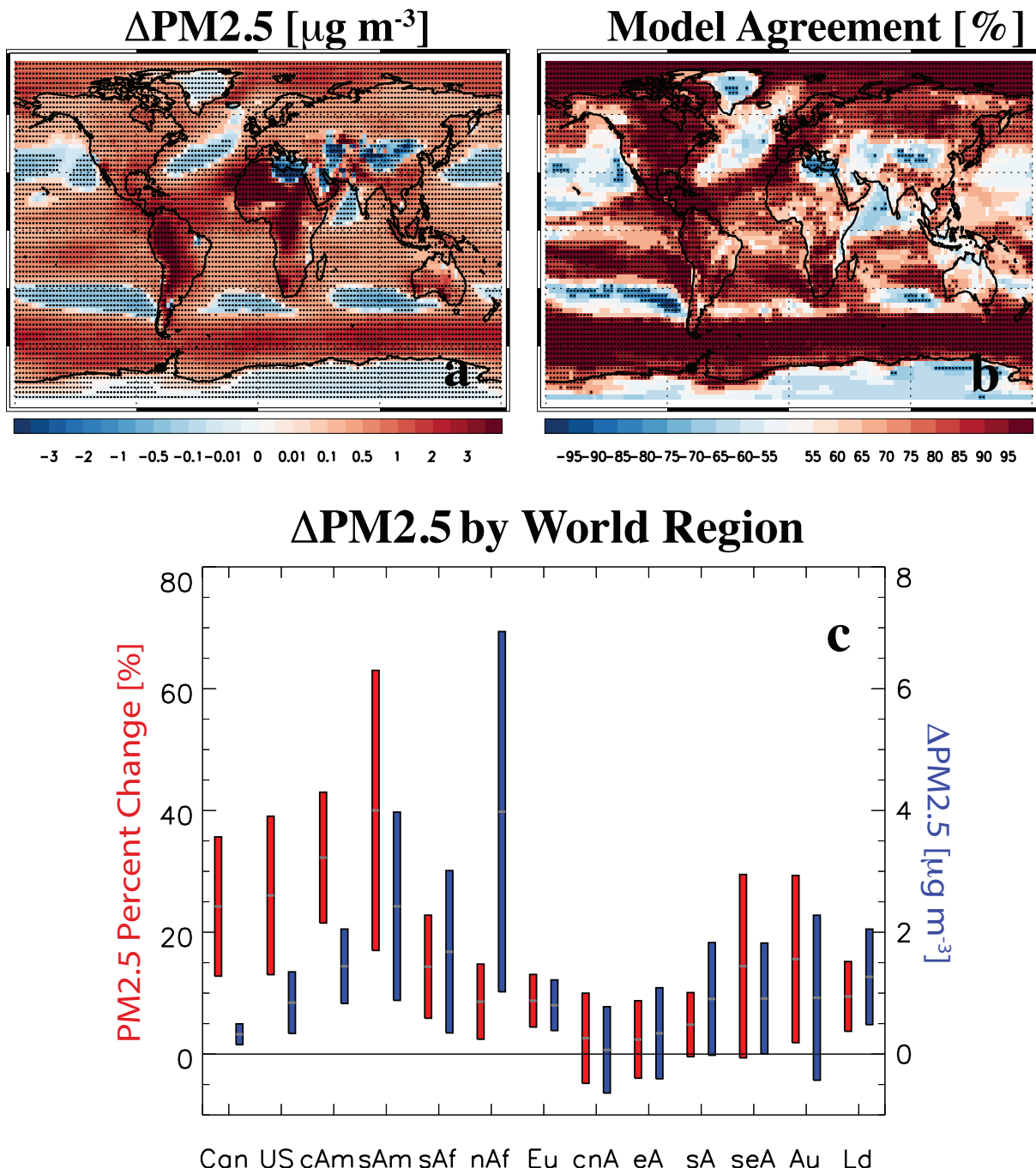


SUPPLEMENTARY FIGURE 14 Additional biosphere responses to GHG-induced warming. Multi-model mean annual mean response of (a) leaf area index (LAI) [dimensionless], (b) net primary productivity of land biomass (NPP) [$\text{kgC km}^{-2} \text{ day}^{-1}$] and (c) CO₂ emissions from fires (fFire) [$\text{kgC km}^{-2} \text{ day}^{-1}$]. Dots in panels (a, b, c) represent a significant response at the 90% confidence level based on a two-tailed pooled *t*-test. Model agreement [%] on the sign of the annual mean response for (d) LAI, (e) NPP and (f) fFire. Dots in panels (d, e, f) represent a significant model agreement at the 90% confidence level based on a two-tailed binomial test. Due to limited data availability (or lack of interactive vegetation/fire), LAI and NPP results are based on 10 models including MPI-ESM-1-2-HAM, GISS-E2-1-G, IPSL-CM5A2-INCA, CESM2-WACCM, CNRM-ESM2-1, GFDL-ESM4, MIROC-ES2L, MRI-ESM2-0, NorESM2-LM, and UKESM1-0-LL; fFire results are based on 5 models including MPI-ESM-1-2-HAM, CESM2-WACCM, CNRM-ESM2-1, MRI-ESM2-0 and NorESM2-LM.



SUPPLEMENTARY FIGURE 15 Archived versus approximated PM_{2.5} in six models. Climatological PM_{2.5} based on (a) archived and (b) approximate PM_{2.5}, and (c) the difference (archived–approximate). PM_{2.5} response (1% per year CO₂ relative to preindustrial) based on (d) archived and (e) approximate PM_{2.5}, and (f) the difference (archived–approximate). Models include GFDL-ESM4, GISS-E2-1-G, MIROC-ES2L, MIROC6, MPI-ESM1-2-HAM and MRI-ESM2-0. Units are $\mu\text{g m}^{-3}$. Dots in (c-f) represent a significant response or difference at the 90% confidence level based on a two-tailed *t*-test.

PM_{2.5} Results Using a Fine Dust Factor of 0.3



SUPPLEMENTARY FIGURE 16 **PM_{2.5} response to GHG-induced warming using a fine dust factor of 0.3.** (a) Multi-model mean annual mean PM_{2.5} response [$\mu\text{g m}^{-3}$]; (b) model agreement on the sign of the PM_{2.5} response [%]; and (c) absolute [$\mu\text{g m}^{-3}$] and relative [%] PM_{2.5} response by world region (regions are identical to those in Figure 1). Note the blue y-axis in (c) for absolute $\Delta\text{PM2.5}$ spans twice the range as that in Figure 1 (all other axes are identical). Dots in (a) represent a significant response at the 90% confidence level based on a two-tailed pooled *t*-test. Red (blue) colors in (b) indicate model agreement on a PM_{2.5} increase (decrease). Dots in (b) represent a significant model agreement at the 90% confidence level based on a two-tailed binomial test. Bar center (gray horizontal line) in (c) shows the multi-model mean response and bar length represents the 90% confidence interval estimated as $\frac{1.65 \times \sigma}{\sqrt{n_m}}$, where σ is the standard deviation across models and n_m is the number of models.

Model/Variant	Experiments Used	Data Reference	Model Reference
CESM2-WACCM	CO ₂ , P, ACO ₂	Danabasoglu, 2019a; Danabasoglu, 2019b; Danabasoglu, 2019c	Danabasoglu et al., 2020
CNRM-ESM2-1	CO ₂ , P, ACO ₂	Seferian, 2018a; Seferian, 2018b; Seferian, 2018c	Séférian et al., 2016; Séférian et al. 2019
GFDL-CM4	CO ₂ , P, ACO ₂	Guo et al., 2018a; Guo et al., 2018b; Guo et al., 2018c	Held et al., 2019
GFDL-ESM4	CO ₂ , P, B, R, ACO ₂	Krasting et al., 2018a; Krasting et al., 2018b; Krasting et al., 2018c; Krasting et al., 2018d; Krasting et al., 2018e	Dunne et al., 2020
GISS-E2-1-G (OMA)	CO ₂ , P, ACO ₂	NASA/GISS, 2018a; NASA/GISS, 2018b; NASA/GISS, 2019c	Kelley et al., 2020; Bauer et al., 2020
HadGEM3-GC31-LL	CO ₂ , P, ACO ₂	Ridley, et al., 2018; Ridley, et al., 2019a Ridley et al., 2019b	Hewitt et al., 2011; Andrews et al., 2020
IPSL-CM5A2-INCA	CO ₂ , P, ACO ₂	Boucher et al., 2020a; Boucher et al., 2020b; Boucher et al., 2021	Sepulchre et al., 2020
MIROC6	CO ₂ , P, ACO ₂	Tatebe & Watanabe, 2018a; Tatebe & Watanabe, 2018b; Tatebe & Watanabe, 2018c	Tatebe et al., 2019
MIROC-ES2L	CO ₂ , P, ACO ₂	Hajima et al., 2019a; Hajima et al., 2019b; Hajima et al., 2019c	Hajima et al., 2020
MPI-ESM-1-2-HAM	CO ₂ , P, ACO ₂	Neubauer et al., 2019a; Neubauer et al., 2019b; Neubauer et al., 2019c	Gutjahr et al., 2019; Neubauer et al., 2019d; Tegen et al., 2019
MRI-ESM2-0	CO ₂ , P, ACO ₂	Yukimoto et al., 2019a;	Yukimoto et al., 2019d

		Yukimoto et al., 2019b; Yukimoto et al., 2019c	
NorESM2-LM	CO2, P, B, R, ACO2	Seland et al., 2019a; Seland et al., 2019b; Seland et al., 2019c; Schwinger et al., 2020a; Schwinger et al., 2020b	Seland et al., 2020
UKESM1-0-LL	CO2, P, B, R, ACO2	Tang et al., 2019a; Tang et al., 2019b; Tang et al., 2019c; Jones, 2019a; Jones, 2019b	Sellar et al., 2019

Supplementary Table 1. CMIP6 models used in this study. Experiments are abbreviated as CO2 = 1% per year CO2; P = preindustrial control; B = 1% per year CO2 biogeochemically coupled only; R= 1% per year CO2 radiatively coupled only; ACO2 = abrupt 4xCO2.

Model/Variant	Horizontal Resolution	Vertical Levels	Aerosol scheme	Natural Sources	SOA Treatment	Chemistry Scheme	Chemistry reactions	BVOCs	Reference
CESM2-WACCM (r1i1p1f1)	0.9° x 1.25°	L70(6x10 ⁶ hPa)	MAM4 (modal scheme, simulating mass and number concentrations) with VBS-SOA	Prescribed climatology of DMS seawater concentrations and emissions. Online emissions of sea-salt and dust aerosols. NOx calculated from lightning. Soil NOx and ocean CO, VOCs from POET	Explicit calculation of SOA using volatility basis set (VBS) where aromatic species, terpenes and isoprene are oxidised to produce a range of gas-phase SOA precursors with different volatilities. Formation of SOA linked to BVOCs emissions from interactive land surface scheme.	MOZART-TSMLT1 covering troposphere, stratosphere, mesosphere and lower thermosphere	231 gas-phase species, 150 photolytic reactions, 403 kinetic reactions and 30 heterogeneous reactions involving ClO _x , BrO _x , NO _x -HO _x -O _x , CO, CH ₄ and NMVOCs	Online biogenic emissions (isoprene, monoterpenes, acetone, methanol, and other short and long-chained hydrocarbons) from dynamically evolving vegetation computed in the Community Land Model (CLM) using the MEGAN2.1 algorithm, which has dependence on light and temperature but also inhibits isoprene emissions based on CO ₂ .	Guenther et al., 2012 (for MEGAN2.1); Liu et al. (2016); Danabasoglu et al., 2020
CNRM-ESM2 (r1i1p1f2)	1.4° x 1.4°	L91 (80km)	TACTIC_v2. Tropospheric aerosols. Mass based aerosol scheme.	Prescribed DMS seawater concentrations. Online emissions of sea-salt and dust aerosols	Prescribed SOA from monthly inventory	No representation of lower tropospheric chemistry.	N/A	N/A	Michou et al., 2020; Michou et al., 2015
GFDL-CM4 (r1i1p1f1)	cubed-sphere (c96) grid, with ~100 km native resolution, regressed to 1.0° x 1.25°	L33(1hPa)	Mass based scheme. Size distribution is prescribed as lognormal for all aerosols except dust and sea salt, which are discretized into five size bins from 0.1-10 μm	Sea salt and dust are parametrized as a function of wind speed.	SOA produced by terrestrial and oceanic sources. Terrestrial production includes natural and anthropogenic sources. The natural source includes oxidation of terpenes emitted from plants, which yields particulate organics	Interactive stratosphere-troposphere (simplified chemistry to simulate aerosols).	Reactions involving SO ₂ , DMS and SO ₄ , including aqueous phase.	N/A	Held et al., 2019

GFDL-ESM4 (r1i1p1f1)	cubed-sphere (c96) grid, with ~100 km native resolution, regressed to 1.0° x 1.25°	L49 (0.01 hPa)	Bulk mass-based scheme. 5 size bins are used for sea salt and dust.	DMS and sea salt emissions calculated online as a function of wind speed and temperature (and a prescribed DMS seawater climatology). Sea salt emissions include an explicit temperature dependence. Dust emissions coupled to interactive vegetation. Lightning NOx calculated online as a function of convection. Natural emissions of NOx, CO, NMVOCs, H2, and NH3 from POET. NH3 from seabird colonies. Two-way exchange of NH3 with ocean.	SOA simulated using an anthropogenic source from oxidation of C4H10 tracer and a prescribed 10% yield from calculated isoprene and terpene emissions from vegetation	Interactive stratosphere-troposphere	43 photolysis reactions, 190 gas-phase kinetic reactions and 15 heterogeneous reactions. NOx-HOx-Ox-chemical cycles and CO, CH4 and NMVOC oxidation reactions	Online emissions of BVOCs (isoprene and monoterpenes) calculated from vegetation cover using MEGAN2.1 algorithm, which has dependence on light and temperature. Inhibition of isoprene emissions is not included	Horowitz et al., 2020
GISS-E2-1-G (r1i1p3f1)	2° x 2.5°	L40 (0.1 hPa)	OMA (one moment aerosol scheme – mass based)	Sea salt, DMS, isoprene and dust emission fluxes are calculated interactively. Online NOx calculated from lightning. Soil NOx, ocean CO, VOCs from GEIA. NH3 from oceans. SO2 from volcanoes as in AeroCom.	Two-product model approximation to represent SOA formation from the oxidation of biogenic VOCs, including NOx dependent chemistry yields	Coupled troposphere-stratosphere chemistry scheme. Modified Carbon Bond Mechanism 4 (CBM-4) chemical mechanism	inorganic chemistry of Ox, NOx, HOx, CO, and organic chemistry of CH4 and lumped higher hydrocarbons (only isoprene and terpenes are explicitly taken into account), along with Cl and Br stratospheric chemistry and heterogenous reactions on PSCs and SO4 aerosols.	Emissions of isoprene from dynamically evolving vegetation are calculated interactively using the algorithm of Guenther et al., (1995), which has dependence on light and temperature. Terpene emissions are prescribed.	Bauer et al., 2020

HadGEM3-GC31 (r1i1p1f3)	1.25° x 1.875°	L85 (85km)	GLOMAP-Mode. (Modal scheme, mass and number). Mass based bin scheme used for dust	Prescribed climatologies of DMS seawater concentrations and BVOC emissions. No marine source of primary organics. Online emissions of sea-salt and dust aerosols	Fixed yield of SOA of 26% calculated from gas-phase oxidation reactions involving prescribed land- based monoterpene sources	Simplified sulphur chemistry for use with aerosol scheme	Oxidation for SO4 and simplified oxidation scheme (monoterpenes) for SOA	N/A	Mulcahy et al., 2020; Tang et al., 2020; Hewitt et al., 2011
IPSL-CM5A2-INCA (r1i1p1f1)	3.75°x1.875°	L39	INCA	Dust and sea salt emissions are parameterized by wind speed. Dust is insoluble.	Explicit secondary organic aerosol formation is not calculated	Tropospheric and stratospheric gas-phase and aerosol- phase chemistry.	Includes 234 homogeneous chemical reactions, 43 photolytic reactions and 30 heterogeneous reactions.	Emissions of isoprene from dynamically evolving vegetation are calculated interactively using the algorithm of Guenther et al., (1995), which has dependence on light and temperature. These are adapted in the ORCHIDEE model	Terrenoire et al., 2022; Lathiere et al., 2006; Folberth et al., 2006
MIROC6 (r1i1p1f1)	1.4°x1.4°	L62	SPRINTARS	Online emissions of DMS, sea-salt and dust aerosols. Primary marine organic aerosol emissions coupled to ocean biogeochemistry.	Prescribed emissions of isoprene and terpenes from GEIA used to convert to secondary organic carbon.	Simplified chemistry for use with aerosol scheme	Oxidation for SO4 and simplified oxidation scheme (isoprene and monoterpenes) for SOA	Prescribed emissions of isoprene and terpenes from GEIA.	Tatebe et al., 2019; Takemura, 2005
MIROC-ES2L (r1i1p1f2)	2.813° x 2.813°	L40 (3.0 hPa)	SPRINTARS	Online emissions of DMS, sea-salt and dust aerosols. Primary marine organic aerosol emissions coupled to ocean biogeochemistry.	Prescribed emissions of isoprene and terpenes from GEIA used to convert to secondary organic carbon.	Simplified chemistry for use with aerosol scheme	Oxidation for SO4 and simplified oxidation scheme (isoprene and monoterpenes) for SOA	Prescribed emissions of isoprene and terpenes from GEIA.	Hajima et al., 2020; Takemura, 2005

MPI-ESM-1-2-HAM (r1i1p1f1)	1.875° x 1.875°	L47 (0.01 hPa)	HAM2.3 (Modal scheme, mass and number)	Interactive online emissions of DMS (using prescribed sea water concentrations), sea- salt and dust aerosols dependent on meteorology	15% of natural terpene emissions at the surface (prescribed) form SOA. SOA have identical properties to primary organic aerosols	Simplified sulphur chemistry. Other fields prescribed.	Reactions involving SO ₂ , DMS and SO ₄ , including aqueous phase.	N/A	Tegen et al., 2019
MRI-ESM2-0 (r1i1p1f1)	MRI- AGCM3.5: 1.125° x 1.125°, MASINGAR mk-2r4c: 1.875° x 1.875°, MRI- CCM2.1: 2.813° x 2.813°	L80 (0.01 hPa)	MASINGAR mk- 2r4c	Interactive online emissions of DMS (using prescribed Climatological DMS sea water concentrations), sea- salt, and dust aerosols dependent on meteorology. Online NO _x calculated from lightning. Climatological soil NO _x and ocean CO, VOCs emissions.	No explicit calculation: 14% of prescribed monoterpene and 1.68 % of isoprene emissions are assumed to form SOA.	Chemistry Climate Model version 2.1 (MRI- CCM2.1) covering troposphere, stratosphere, and mesosphere	90 chemical species and 259 chemical reactions (184 gas-phase reactions, 59 photolysis reactions, and 16 heterogeneous reactions) involving HO _x -NO _x - CH ₄ -CO cycles and NMVOC oxidation reactions, and halogen chemistry (Cl and Br)	Climatological BVOCs emissions	Deushi and Shibata, 2011; Yukimoto et al., 2019d
NorESM2-LM (r1i1p1f1)	1.9° x 2.5°	L32 (3.64 hPa)	OsloAero6	Interactive emissions for sea- salt, biogenic primary OM (including MSA) and DMS over oceans, and interactive mineral dust and BVOC over land	Fixed SOA formation yields of 15% and 5% from oxidation of monoterpene and isoprene	Simplified chemistry for use in aerosol scheme. Other fields prescribed	Oxidation for SO ₄ and simplified oxidation scheme (isoprene and monoterpene) for SOA	Online biogenic emissions from dynamically evolving vegetation computed in the Community Land Model (CLM) using the MEGAN2.1 algorithm, which has dependence on light and temperature but also inhibits isoprene emissions based on CO ₂ .	Kirkevåg et al., 2018; Selend et al., 2020

UKESM1-0-LL (r1i1p1f2)	1.25° x 1.875°	L85 (85km)	GLOMAP-Mode. (Modal scheme, mass and number). Mass based bin scheme used for dust.	Dynamic vegetation and interactive ocean biogeochemistry used for online emissions of DMS, sea-salt and dust aerosols, as well as emissions of primary marine organics and biogenic organic compounds. Online NOx calculated from lightning, soil NOx and ocean CO, VOCs from POET	Fixed SOA yield of 26% from gas- phase oxidation reactions involving interactive land-based monoterpene sources.	UKCA coupled stratosphere- troposphere. Interactive photolysis	84 chemical tracers. Simulates chemical cycles of Ox, HOx and NOx, as well as oxidation reactions of CO, CH4 and NMVOCs. In addition, heterogeneous processes, Cl and Br chemistry are included.	Dynamic vegetation and land surface model used to calculate interactive emissions of Isoprene and monoterpenes using light and temperature, but isoprene emissions are inhibited based on CO2. Isoprene emissions coupled to chemistry and affect tropospheric O3 and methane lifetime. Monoterpenes only affect SOA.	Mulcahy et al., 2020; Tang et al., 2020; Archibald et al., 2020
------------------------	----------------	---------------	---	--	--	--	---	---	---

Supplementary Table 2: CMIP6 model descriptions of resolution, aerosol schemes, and treatment of important processes, including chemistry, secondary organic aerosol and BVOC emissions.

Supplementary References

- Allen, R. J., Landuyt, W. & Rumbold, S. (2016). An increase in aerosol burden and radiative effects in a warmer world. *Nature Clim Change* **6**, 269–274. <https://doi.org/10.1038/nclimate2827>
- Andrews, M. B., Ridley, J. K., Wood, R. A., Andrews, T., Blockley, E. W., Booth, B., et al. (2020). Historical simulations with HadGEM3-GC3.1 for CMIP6. *Journal of Advances in Modeling Earth Systems*, **12**, e2019MS001995. <https://doi.org/10.1029/2019MS001995>
- Archibald, A. T., O'Connor, F. M., Abraham, N. L., Archer-Nicholls, S., Chipperfield, M. P., Dalvi, M., Folberth, G. A., Dennison, F., Dhomse, S. S., Griffiths, P. T., Hardacre, C., Hewitt, A. J., Hill, R. S., Johnson, C. E., Keeble, J., Köhler, M. O., Morgenstern, O., Mulcahy, J. P., Ordóñez, C., Pope, R. J., Rumbold, S. T., Russo, M. R., Savage, N. H., Sellar, A., Stringer, M., Turnock, S. T., Wild, O., and Zeng, G. (2020). Description and evaluation of the UKCA stratosphere–troposphere chemistry scheme (StratTrop vn 1.0) implemented in UKESM1, *Geosci. Model Dev.*, **13**, 1223–1266, <https://doi.org/10.5194/gmd-13-1223-2020>
- Arneth, A., Niinemets, Ü., Pressley, S., Bäck, J., Hari, P., Karl, T., Noe, S., Prentice, I. C., Serça, D., Hickler, T., Wolf, A., and Smith, B. (2007). Process-based estimates of terrestrial ecosystem isoprene emissions: incorporating the effects of a direct CO₂-isoprene interaction, *Atmos. Chem. Phys.*, **7**, 31–53, <https://doi.org/10.5194/acp-7-31-2007>
- Bauer, S. E., Tsigaridis, K., Faluvegi, G., Kelley, M., Lo, K. K., Miller, R. L., Nazarenko, L., Schmidt, G. A., and Wu, J. (2020). Historical (1850–2014) aerosol evolution and role on climate forcing using the GISS ModelE2.1 contribution to CMIP6. *J. Adv. Model. Earth Syst.*, **12**, no. 8, e2019MS001978, doi:10.1029/2019MS001978
- Boucher, O., Denvil, S., Levavasseur, G., Cozic, A., Caubel, A., Foujols, M.-A., Meurdesoif, Y., Balkanski, Y., Checa-Garcia, R., Hauglustaine, D., Bekki, S., & Marchand, M. (2020a). IPSL IPSL-CM5A2-INCA model output prepared for CMIP6 CMIP 1pctCO₂ (Version 20220607) [Application/x-netcdf]. Earth System Grid Federation. <https://doi.org/10.22033/ESGF/CMIP6.13643>
- Boucher, O., Denvil, S., Levavasseur, G., Cozic, A., Caubel, A., Foujols, M.-A., Meurdesoif, Y., Balkanski, Y., Checa-Garcia, R., Hauglustaine, D., Bekki, S., & Marchand, M. (2020b). IPSL IPSL-CM5A2-INCA model output prepared for CMIP6 CMIP abrupt-4xCO₂ (Version 20220607) [Application/x-netcdf]. Earth System Grid Federation. <https://doi.org/10.22033/ESGF/CMIP6.13644>
- Boucher, O., Denvil, S., Levavasseur, G., Cozic, A., Caubel, A., Foujols, M.-A., Meurdesoif, Y., Balkanski, Y., Checa-Garcia, R., Hauglustaine, D., Bekki, S., & Marchand, M. (2021). IPSL IPSL-CM5A2-INCA model output prepared for CMIP6 CMIP piControl (Version 20220607) [Application/x-netcdf]. Earth System Grid Federation. <https://doi.org/10.22033/ESGF/CMIP6.13683>

- Danabasoglu, G. (2019a). NCAR CESM2-WACCM model output prepared for CMIP6 CMIP piControl (Version 20220616) [Application/x-netcdf]. Earth System Grid Federation. <https://doi.org/10.22033/ESGF/CMIP6.10094>
- Danabasoglu, G. (2019b). NCAR CESM2-WACCM model output prepared for CMIP6 CMIP 1pctCO₂ (Version 20220616) [Application/x-netcdf]. Earth System Grid Federation. <https://doi.org/10.22033/ESGF/CMIP6.10028>
- Danabasoglu, G. (2019c). NCAR CESM2-WACCM model output prepared for CMIP6 CMIP abrupt-4xCO₂ (Version 20220616) [Application/x-netcdf]. Earth System Grid Federation. <https://doi.org/10.22033/ESGF/CMIP6.10039>
- Danabasoglu, G., Lamarque, J.-F., Bacmeister, J., Bailey, D. A., DuVivier, A. K., Edwards, J., Emmons, L. K., Fasullo, J., Garcia, R., Gettelman, A., Hannay, C., Holland, M. M., Large, W. G., Lauritzen, P. H., Lawrence, D. M., Lenaerts, J. T. M., Lindsay, K., Lipscomb, W. H., Mills, M. J., ... Strand, W. G. (2020). The Community Earth System Model Version 2 (CESM2). *Journal of Advances in Modeling Earth Systems*, 12(2), e2019MS001916. <https://doi.org/10.1029/2019MS001916>
- Deushi, M., & Shibata, K. (2011). Impacts of increases in greenhouse gases and ozone recovery on lower stratospheric circulation and the age of air: Chemistry-climate model simulations up to 2100. *Journal of Geophysical Research: Atmospheres*, 116(D7). <https://doi.org/10.1029/2010JD015024>
- Dunne, J. P., Horowitz, L. W., Adcroft, A. J., Ginoux, P., Held, I. M., John, J. G., Krasting, J. P., Malyshev, S., Naik, V., Paulot, F., Shevliakova, E., Stock, C. A., Zadeh, N., Balaji, V., Blanton, C., Dunne, K. A., Dupuis, C., Durachta, J., Dussin, R., ... Zhao, M. (2020). The GFDL Earth System Model Version 4.1 (GFDL-ESM 4.1): Overall Coupled Model Description and Simulation Characteristics. *Journal of Advances in Modeling Earth Systems*, 12(11), e2019MS002015. <https://doi.org/10.1029/2019MS002015>
- Folberth, G. A., Hauglustaine, D. A., Lathière, J., & Brocheton, F. (2006). Interactive chemistry in the Laboratoire de Météorologie Dynamique general circulation model: Model description and impact analysis of biogenic hydrocarbons on tropospheric chemistry. *Atmospheric Chemistry and Physics*, 6(8), 2273–2319. <https://doi.org/10.5194/acp-6-2273-2006>
- Guenther, A. B., Jiang, X., Heald, C. L., Sakulyanontvittaya, T., Duhl, T., Emmons, L. K., & Wang, X. (2012). The Model of Emissions of Gases and Aerosols from Nature version 2.1 (MEGAN2.1): An extended and updated framework for modeling biogenic emissions. *Geoscientific Model Development*, 5(6), 1471–1492. <https://doi.org/10.5194/gmd-5-1471-2012>
- Guenther, A., Hewitt, C. N., Erickson, D., Fall, R., Geron, C., Graedel, T., Harley, P., Klinger, L., Lerdau, M., Mckay, W. A., Pierce, T., Scholes, B., Steinbrecher, R., Tallamraju, R., Taylor, J., & Zimmerman, P. (1995). A global model of natural volatile organic compound emissions. *Journal of Geophysical Research: Atmospheres*, 100(D5), 8873–8892. <https://doi.org/10.1029/94JD02950>

Guo, H., John, J. G., Blanton, C., McHugh, C., Nikonorov, S., Radhakrishnan, A., Rand, K., Zadeh, N. T., Balaji, V., Durachta, J., Dupuis, C., Menzel, R., Robinson, T., Underwood, S., Vahlenkamp, H., Bushuk, M., Dunne, K. A., Dussin, R., Gauthier, P. P., ... Zhang, R. (2018a). NOAA-GFDL GFDL-CM4 model output 1pctCO₂ (Version 20220609) [Application/x-netcdf]. Earth System Grid Federation. <https://doi.org/10.22033/ESGF/CMIP6.8470>

Guo, H., John, J. G., Blanton, C., McHugh, C., Nikonorov, S., Radhakrishnan, A., Rand, K., Zadeh, N. T., Balaji, V., Durachta, J., Dupuis, C., Menzel, R., Robinson, T., Underwood, S., Vahlenkamp, H., Bushuk, M., Dunne, K. A., Dussin, R., Gauthier, P. P., ... Zhang, R. (2018b). NOAA-GFDL GFDL-CM4 model output piControl (Version 20220609) [Application/x-netcdf]. Earth System Grid Federation. <https://doi.org/10.22033/ESGF/CMIP6.8666>

Guo, H., John, J. G., Blanton, C., McHugh, C., Nikonorov, S., Radhakrishnan, A., Rand, K., Zadeh, N. T., Balaji, V., Durachta, J., Dupuis, C., Menzel, R., Robinson, T., Underwood, S., Vahlenkamp, H., Bushuk, M., Dunne, K. A., Dussin, R., Gauthier, P. P., ... Zhang, R. (2018c). NOAA-GFDL GFDL-CM4 model output piControl (Version 20220609) [Application/x-netcdf]. Earth System Grid Federation. <https://doi.org/10.22033/ESGF/CMIP6.8486>

Gutjahr, O., Putrasahan, D., Lohmann, K., Jungclaus, J. H., von Storch, J.-S., Brüggemann, N., Haak, H., & Stössel, A. (2019). Max Planck Institute Earth System Model (MPI-ESM1.2) for the High-Resolution Model Intercomparison Project (HighResMIP). *Geoscientific Model Development*, 12(7), 3241–3281. <https://doi.org/10.5194/gmd-12-3241-2019>

Hajima, T., Abe, M., Arakawa, O., Suzuki, T., Komuro, Y., Ogura, T., Ogochi, K., Watanabe, M., Yamamoto, A., Tatebe, H., Noguchi, M. A., Ohgaito, R., Ito, A., Yamazaki, D., Ito, A., Takata, K., Watanabe, S., Kawamiya, M., & Tachiiri, K. (2019a). MIROC MIROC-ES2L model output prepared for CMIP6 CMIP 1pctCO₂ (Version 20220621) [Application/x-netcdf]. Earth System Grid Federation. <https://doi.org/10.22033/ESGF/CMIP6.5370>

Hajima, T., Abe, M., Arakawa, O., Suzuki, T., Komuro, Y., Ogura, T., Ogochi, K., Watanabe, M., Yamamoto, A., Tatebe, H., Noguchi, M. A., Ohgaito, R., Ito, A., Yamazaki, D., Ito, A., Takata, K., Watanabe, S., Kawamiya, M., & Tachiiri, K. (2019b). MIROC MIROC-ES2L model output prepared for CMIP6 CMIP piControl (Version 20220621) [Application/x-netcdf]. Earth System Grid Federation. <https://doi.org/10.22033/ESGF/CMIP6.5710>

Hajima, T., Abe, M., Arakawa, O., Suzuki, T., Komuro, Y., Ogura, T., Ogochi, K., Watanabe, M., Yamamoto, A., Tatebe, H., Noguchi, M. A., Ohgaito, R., Ito, A., Yamazaki, D., Ito, A., Takata, K., Watanabe, S., Kawamiya, M., & Tachiiri, K. (2019c). MIROC MIROC-ES2L model output prepared for CMIP6 CMIP abrupt-4xCO₂ (Version 20220621) [Application/x-netcdf]. Earth System Grid Federation.

<https://doi.org/10.22033/ESGF/CMIP6.5410>

Hajima, T., Watanabe, M., Yamamoto, A., Tatebe, H., Noguchi, M. A., Abe, M., Ohgaito, R., Ito, A., Yamazaki, D., Okajima, H., Ito, A., Takata, K., Ogochi, K., Watanabe, S., & Kawamiya, M. (2020). Development of the MIROC-ES2L Earth system model and the evaluation of biogeochemical processes and feedbacks. *Geoscientific Model Development*, 13(5), 2197–2244. <https://doi.org/10.5194/gmd-13-2197-2020>

Held, I. M., Guo, H., Adcroft, A., Dunne, J. P., Horowitz, L. W., Krasting, J., et al. (2019). Structure and performance of GFDL's CM4.0 climate model. *Journal of Advances in Modeling Earth Systems*, 11, 3691–3727, doi: 10.1029/2019MS001829.

Hewitt, H. T., Copsey, D., Culverwell, I. D., Harris, C. M., Hill, R. S. R., Keen, A. B., McLaren, A. J., & Hunke, E. C. (2011). Design and implementation of the infrastructure of HadGEM3: The next-generation Met Office climate modelling system. *Geoscientific Model Development*, 4(2), 223–253. <https://doi.org/10.5194/gmd-4-223-2011>

Horowitz, L. W., Naik, V., Paulot, F., Ginoux, P. A., Dunne, J. P., & Mao, J., et al. (2020). The GFDL global atmospheric chemistry-climate model AM4.1: Model description and simulation characteristics. *Journal of Advances in Modeling Earth Systems*, 12, e2019MS002032, doi: 10.1029/2019MS002032

Jones, Chris (2019a). *MOHC UKESM1.0-LL model output prepared for CMIP6 C4MIP 1pctCO2-bgc* (Version 20220609). Earth System Grid Federation. <https://doi.org/10.22033/ESGF/CMIP6.5796>

Jones, Chris (2019b). *MOHC UKESM1.0-LL model output prepared for CMIP6 C4MIP 1pctCO2-rad* (Version 20220609). Earth System Grid Federation. <https://doi.org/10.22033/ESGF/CMIP6.5800>

Kelley, M., Schmidt, G. A., Nazarenko, L. S., Bauer, S. E., Ruedy, R., Russell, G. L., Ackerman, A. S., Aleinov, I., Bauer, M., Bleck, R., Canuto, V., Cesana, G., Cheng, Y., Clune, T. L., Cook, B. I., Cruz, C. A., Del Genio, A. D., Elsaesser, G. S., Faluvegi, G., ... Yao, M. (2020). GISS-E2.1: Configurations and Climatology. *Journal of Advances in Modeling Earth Systems*, 12(8). <https://doi.org/10.1029/2019MS002025>

Kirkevåg, A., Grini, A., Olivié, D., Seland, Ø., Alterskjær, K., Hummel, M., Karset, I. H. H., Lewinschal, A., Liu, X., Makkonen, R., Bethke, I., Griesfeller, J., Schulz, M., and Iversen, T. (2018). A production-tagged aerosol module for Earth system models, OsloAero5.3 – extensions and updates for CAM5.3-Oslo, *Geosci. Model Dev.*, 11, 3945–3982, <https://doi.org/10.5194/gmd-11-3945-2018>

Krasting, J. P., Blanton, C., McHugh, C., Radhakrishnan, A., John, J. G., Rand, K., Nikonov, S., Vahlenkamp, H., Zadeh, N. T., Dunne, J. P., Shevliakova, E., Horowitz, L. W., Stock, C., Malyshev, S., Poshay, J., Gauthier, P. P., Naik, V., Winton, M., & Zeng, Y. (2018a). NOAA-GFDL GFDL-ESM4 model output prepared for CMIP6 C4MIP 1pctCO2-bgc (Version 20220609) [Application/x-netcdf]. Earth System Grid Federation. <https://doi.org/10.22033/ESGF/CMIP6.8475>

Krasting, J. P., Blanton, C., McHugh, C., Radhakrishnan, A., John, J. G., Rand, K., Nikonov, S., Vahlenkamp, H., Zadeh, N. T., Dunne, J. P., Shevliakova, E., Horowitz, L. W., Stock, C., Malyshev, S., Poshay, J., Gauthier, P. P., Naik, V., Winton, M., & Zeng, Y. (2018b). NOAA-GFDL GFDL-ESM4 model output prepared for CMIP6 C4MIP 1pctCO2-rad (Version 20220609) [Application/x-netcdf]. Earth System Grid Federation. <https://doi.org/10.22033/ESGF/CMIP6.8477>

Krasting, J. P., John, J. G., Blanton, C., McHugh, C., Nikonov, S., Radhakrishnan, A., Rand, K., Zadeh, N. T., Balaji, V., Durachta, J., Dupuis, C., Menzel, R., Robinson, T., Underwood, S., Vahlenkamp, H., Dunne, K. A., Gauthier, P. P., Ginoux, P., Griffies, S. M., ... Zhao, M. (2018c). NOAA-

GFDL GFDL-ESM4 model output prepared for CMIP6 CMIP 1pctCO₂ (Version 20220609) [Application/x-netcdf]. Earth System Grid Federation. <https://doi.org/10.22033/ESGF/CMIP6.8473>

Krasting, J. P., John, J. G., Blanton, C., McHugh, C., Nikonov, S., Radhakrishnan, A., Rand, K., Zadeh, N. T., Balaji, V., Durachta, J., Dupuis, C., Menzel, R., Robinson, T., Underwood, S., Vahlenkamp, H., Dunne, K. A., Gauthier, P. P., Ginoux, P., Griffies, S. M., ... Zhao, M. (2018d). NOAA-GFDL GFDL-ESM4 model output prepared for CMIP6 CMIP piControl (Version 20220609) [Application/x-netcdf]. Earth System Grid Federation. <https://doi.org/10.22033/ESGF/CMIP6.8669>

Krasting, J. P., John, J. G., Blanton, C., McHugh, C., Nikonov, S., Radhakrishnan, A., Rand, K., Zadeh, N. T., Balaji, V., Durachta, J., Dupuis, C., Menzel, R., Robinson, T., Underwood, S., Vahlenkamp, H., Dunne, K. A., Gauthier, P. P., Ginoux, P., Griffies, S. M., ... Zhao, M. (2018e). NOAA-GFDL GFDL-ESM4 model output prepared for CMIP6 CMIP abrupt-4xCO₂ (Version 20220609) [Application/x-netcdf]. Earth System Grid Federation. <https://doi.org/10.22033/ESGF/CMIP6.8489>

Lathiere, J., Hauglustaine, D. A., Friend, A. D., Noblet-Ducoudre, N. D., Viovy, N., & Folberth, G. A. (2006). Impact of climate variability and land use changes on global biogenic volatile organic compound emissions. *Atmos. Chem. Phys.*, 6, 2129–2146, <https://doi.org/10.5194/acp-6-2129-2006>

Liu, X., Ma, P.-L., Wang, H., Tilmes, S., Singh, B., Easter, R. C., Ghan, S. J., and Rasch, P. J. (2016). Description and evaluation of a new four-mode version of the Modal Aerosol Module (MAM4) within version 5.3 of the Community Atmosphere Model, *Geosci. Model Dev.*, 9, 505–522, <https://doi.org/10.5194/gmd-9-505-2016>

Michou, M., Nabat, P., and Saint-Martin, D. (2015). Development and basic evaluation of a prognostic aerosol scheme (v1) in the CNRM Climate Model CNRM-CM6, *Geosci. Model Dev.*, 8, 501–531, <https://doi.org/10.5194/gmd-8-501-2015>

Michou, M., Nabat, P., Saint-Martin, D., Bock, J., Decharme, B., Mallet, M., Roehrig, R., Séférian, R., Sénési, S., & Volodire, A. (2020). Present-Day and Historical Aerosol and Ozone Characteristics in CNRM CMIP6 Simulations. *Journal of Advances in Modeling Earth Systems*, 12(1). <https://doi.org/10.1029/2019MS001816>

Mulcahy, J. P., Johnson, C., Jones, C. G., Povey, A. C., Scott, C. E., Sellar, A., Turnock, S. T., Woodhouse, M. T., Abraham, N. L., Andrews, M. B., Bellouin, N., Browse, J., Carslaw, K. S., Dalvi, M., Folberth, G. A., Glover, M., Grosvenor, D. P., Hardacre, C., Hill, R., Johnson, B., Jones, A., Kipling, Z., Mann, G., Mollard, J., O'Connor, F. M., Palmiéri, J., Reddington, C., Rumbold, S. T., Richardson, M., Schutgens, N. A. J., Stier, P., Stringer, M.,

Pacifico, F., Folberth, G. A., Jones, C. D., Harrison, S. P., and Collins, W. J. (2012). Sensitivity of biogenic isoprene emissions to past, present, and future environmental conditions and implications for atmospheric chemistry, *J. Geophys. Res.*, 117, D22302, doi:10.1029/2012JD018276

NASA Goddard Institute For Space Studies (NASA/GISS). (2018a). NASA-GISS GISS-E2.1G model output prepared for CMIP6 CMIP 1pctCO2 (Version 20220602) [Application/x-netcdf]. Earth System Grid Federation. <https://doi.org/10.22033/ESGF/CMIP6.6950>

NASA Goddard Institute For Space Studies (NASA/GISS). (2018b). NASA-GISS GISS-E2.1G model output prepared for CMIP6 CMIP piControl (Version 20220602) [Application/x-netcdf]. Earth System Grid Federation. <https://doi.org/10.22033/ESGF/CMIP6.7380>

NASA Goddard Institute For Space Studies (NASA/GISS). (2018c). NASA-GISS GISS-E2.1G model output prepared for CMIP6 CMIP abrupt-4xCO2 (Version 20220602) [Application/x-netcdf]. Earth System Grid Federation. <https://doi.org/10.22033/ESGF/CMIP6.6976>

Neubauer, D., Ferrachat, S., Siegenthaler-Le Drian, C., Stoll, J., Folini, D. S., Tegen, I., Wieners, K.-H., Mauritsen, T., Stemmler, I., Barthel, S., Bey, I., Daskalakis, N., Heinold, B., Kokkola, H., Partridge, D., Rast, S., Schmidt, H., Schutgens, N., Stanelle, T., ... Lohmann, U. (2019a). HAMMOZ-Consortium MPI-ESM1.2-HAM model output prepared for CMIP6 CMIP 1pctCO2 (Version 20220602) [Application/x-netcdf]. Earth System Grid Federation. <https://doi.org/10.22033/ESGF/CMIP6.4999>

Neubauer, D., Ferrachat, S., Siegenthaler-Le Drian, C., Stoll, J., Folini, D. S., Tegen, I., Wieners, K.-H., Mauritsen, T., Stemmler, I., Barthel, S., Bey, I., Daskalakis, N., Heinold, B., Kokkola, H., Partridge, D., Rast, S., Schmidt, H., Schutgens, N., Stanelle, T., ... Lohmann, U. (2019b). HAMMOZ-Consortium MPI-ESM1.2-HAM model output prepared for CMIP6 CMIP piControl (Version 20220602) [Application/x-netcdf]. Earth System Grid Federation. <https://doi.org/10.22033/ESGF/CMIP6.5037>

Neubauer, D., Ferrachat, S., Siegenthaler-Le Drian, C., Stoll, J., Folini, D. S., Tegen, I., Wieners, K.-H., Mauritsen, T., Stemmler, I., Barthel, S., Bey, I., Daskalakis, N., Heinold, B., Kokkola, H., Partridge, D., Rast, S., Schmidt, H., Schutgens, N., Stanelle, T., ... Lohmann, U. (2019c). HAMMOZ-Consortium MPI-ESM1.2-HAM model output prepared for CMIP6 CMIP abrupt-4xCO2 (Version 20220602) [Application/x-netcdf]. Earth System Grid Federation. <https://doi.org/10.22033/ESGF/CMIP6.5000>

Neubauer, D., Ferrachat, S., Siegenthaler-Le Drian, C., Stier, P., Partridge, D. G., Tegen, I., Bey, I., Stanelle, T., Kokkola, H., and Lohmann, U. (2019d). The global aerosol-climate model ECHAM6.3–HAM2.3 – Part 2: Cloud evaluation, aerosol radiative forcing, and climate sensitivity, *Geosci. Model Dev.*, 12, 3609–3639, <https://doi.org/10.5194/gmd-12-3609-2019>

Rabin, S. S., Melton, J. R., Lasslop, G., Bachelet, D., Forrest, M., Hantson, S., Kaplan, J. O., Li, F., Mangeon, S., Ward, D. S., Yue, C., Arora, V. K., Hickler, T., Kloster, S., Knorr, W., Nieradzik, L., Spessa, A., Folberth, G. A., Sheehan, T., Voulgarakis, A., Kelley, D. I., Prentice, I. C., Sitch, S., Harrison, S., and Arneth, A. (2017). The Fire Modeling Intercomparison Project (FireMIP), phase 1: experimental and analytical protocols with detailed model descriptions, *Geosci. Model Dev.*, 10, 1175–1197, <https://doi.org/10.5194/gmd-10-1175-2017>

- Ridley, J., Menary, M., Kuhlbrodt, T., Andrews, M., & Andrews, T. (2018). MOHC HadGEM3-GC31-LL model output prepared for CMIP6 CMIP piControl (Version 20220602) [Application/x-netcdf]. Earth System Grid Federation. <https://doi.org/10.22033/ESGF/CMIP6.6294>
- Ridley, J., Menary, M., Kuhlbrodt, T., Andrews, M., & Andrews, T. (2019a). MOHC HadGEM3-GC31-LL model output prepared for CMIP6 CMIP 1pctCO2 (Version 20220602) [Application/x-netcdf]. Earth System Grid Federation. <https://doi.org/10.22033/ESGF/CMIP6.5788>
- Ridley, J., Menary, M., Kuhlbrodt, T., Andrews, M., & Andrews, T. (2019b). MOHC HadGEM3-GC31-LL model output prepared for CMIP6 CMIP abrupt-4xCO2 (Version 20220602) [Application/x-netcdf]. Earth System Grid Federation. <https://doi.org/10.22033/ESGF/CMIP6.5839>
- Seferian, R. (2018a). CNRM-CERFACS CNRM-ESM2-1 model output prepared for CMIP6 CMIP for experiment 1pctCO2 (Version 20220620) [Application/x-netcdf]. Earth System Grid Federation. <https://doi.org/10.22033/ESGF/CMIP6.3714>
- Seferian, R. (2018b). CNRM-CERFACS CNRM-ESM2-1 model output prepared for CMIP6 CMIP piControl (Version 20220620) [Application/x-netcdf]. Earth System Grid Federation. <https://doi.org/10.22033/ESGF/CMIP6.4165>
- Seferian, R. (2018c). CNRM-CERFACS CNRM-ESM2-1 model output prepared for CMIP6 CMIP abrupt-4xCO2 (Version 20220620) [Application/x-netcdf]. Earth System Grid Federation. <https://doi.org/10.22033/ESGF/CMIP6.3918>
- Séférian, R., Delire, C., Decharme, B., Volodko, A., Salas y Melia, D., Chevallier, M., Saint-Martin, D., Aumont, O., Calvet, J.-C., Carrer, D., Douville, H., Franchistéguy, L., Joetzjer, E., & Sénési, S. (2016). Development and evaluation of CNRM Earth system model – CNRM-ESM1. *Geoscientific Model Development*, 9(4), 1423–1453. <https://doi.org/10.5194/gmd-9-1423-2016>
- Séférian, R., Nabat, P., Michou, M., Saint-Martin, D., Volodko, A., Colin, J., et al (2019). Evaluation of CNRM Earth-System model, CNRM-ESM2-1: role of Earth system processes in present-day and future climate. *Journal of Advances in Modeling Earth Systems*, 11, 4182–4227. <https://doi.org/10.1029/2019MS001791>
- Seland, Ø., Bentsen, M., Olivière, D. J. L., Toniazzo, T., Gjermundsen, A., Graff, L. S., Debernard, J. B., Gupta, A. K., He, Y., Kirkevåg, A., Schwinger, J., Tjiputra, J., Aas, K. S., Bethke, I., Fan, Y., Griesfeller, J., Grini, A., Guo, C., Ilicak, M., ... Schulz, M. (2019a). NCC NorESM2-LM model output prepared for CMIP6 CMIP 1pctCO2 (Version 20220609) [Application/x-netcdf]. Earth System Grid Federation. <https://doi.org/10.22033/ESGF/CMIP6.7802>
- Seland, Ø., Bentsen, M., Olivière, D. J. L., Toniazzo, T., Gjermundsen, A., Graff, L. S., Debernard, J. B., Gupta, A. K., He, Y., Kirkevåg, A., Schwinger, J., Tjiputra, J., Aas, K. S., Bethke, I., Fan, Y., Griesfeller, J., Grini, A., Guo, C., Ilicak, M., ... Schulz, M. (2019b). NCC NorESM2-LM model output prepared for CMIP6 CMIP piControl (Version 20220609) [Application/x-netcdf]. Earth System Grid Federation. <https://doi.org/10.22033/ESGF/CMIP6.8217>

Seland, Ø., Bentsen, M., Olivière, D. J. L., Toniazzo, T., Gjermundsen, A., Graff, L. S., Debernard, J. B., Gupta, A. K., He, Y., Kirkevåg, A., Schwinger, J., Tjiputra, J., Aas, K. S., Bethke, I., Fan, Y., Griesfeller, J., Grini, A., Guo, C., Ilicak, M., ... Schulz, M. (2019c). NCC NorESM2-LM model output prepared for CMIP6 CMIP abrupt-4xCO₂ (Version 20220609) [Application/x-netcdf]. Earth System Grid Federation. <https://doi.org/10.22033/ESGF/CMIP6.7836>

Seland, Ø., Bentsen, M., Olivière, D., Toniazzo, T., Gjermundsen, A., Graff, L. S., Debernard, J. B., Gupta, A. K., He, Y.-C., Kirkevåg, A., Schwinger, J., Tjiputra, J., Aas, K. S., Bethke, I., Fan, Y., Griesfeller, J., Grini, A., Guo, C., Ilicak, M., ... Schulz, M. (2020). Overview of the Norwegian Earth System Model (NorESM2) and key climate response of CMIP6 DECK, historical, and scenario simulations. *Geoscientific Model Development*, 13(12), 6165–6200. <https://doi.org/10.5194/gmd-13-6165-2020>

Sellar, A. A., Jones, C. G., Mulcahy, J. P., Tang, Y., Yool, A., Wiltshire, A., O'Connor, F. M., Stringer, M., Hill, R., Palmieri, J., Woodward, S., de Mora, L., Kuhlbrodt, T., Rumbold, S. T., Kelley, D. I., Ellis, R., Johnson, C. E., Walton, J., Abraham, N. L., ... Zerroukat, M. (2019). UKESM1: Description and Evaluation of the U.K. Earth System Model. *Journal of Advances in Modeling Earth Systems*, 11(12), 4513–4558. <https://doi.org/10.1029/2019MS001739>

Sepulchre, P., Caubel, A., Ladant, J.-B., Bopp, L., Boucher, O., Braconnot, P., Brockmann, P., Cozic, A., Donnadieu, Y., Dufresne, J.-L., Estella-Perez, V., Ethé, C., Fluteau, F., Foujols, M.-A., Gastineau, G., Ghattas, J., Hauglustaine, D., Hourdin, F., Kageyama, M., ... Tardif, D. (2020). IPSL-CM5A2 – an Earth system model designed for multi-millennial climate simulations. *Geoscientific Model Development*, 13(7), 3011–3053. <https://doi.org/10.5194/gmd-13-3011-2020>

Schwinger, Jörg; Tjiputra, Jerry; Seland, Øyvind; Bentsen, Mats; Olivière, Dirk Jan Leo; Toniazzo, Thomas; Gjermundsen, Ada; Graff, Lise Seland; Debernard, Jens Boldingh; Gupta, Alok Kumar; He, Yanchun; Kirkevåg, Alf; Aas, Kjetil Schanke; Bethke, Ingo; Fan, Yuanchao; Gao, Shuang; Griesfeller, Jan; Grini, Alf; Guo, Chuncheng; Ilicak, Mehmet; Karset, Inger Helene Hafsaahl; Liakka, Johan; Moseid, Kine Onsum; Nummelin, Aleksi; Tang, Hui; Zhang, Zhongshi; Heinze, Christoph; Iversen, Trond; Schulz, Michael (2020a). *NCC NorESM2-LM model output prepared for CMIP6 C4MIP 1pctCO₂-rad* (Version 20220602). Earth System Grid Federation. <https://doi.org/10.22033/ESGF/CMIP6.13726>

Schwinger, Jörg; Tjiputra, Jerry; Seland, Øyvind; Bentsen, Mats; Olivière, Dirk Jan Leo; Toniazzo, Thomas; Gjermundsen, Ada; Graff, Lise Seland; Debernard, Jens Boldingh; Gupta, Alok Kumar; He, Yanchun; Kirkevåg, Alf; Aas, Kjetil Schanke; Bethke, Ingo; Fan, Yuanchao; Gao, Shuang; Griesfeller, Jan; Grini, Alf; Guo, Chuncheng; Ilicak, Mehmet; Karset, Inger Helene Hafsaahl; Liakka, Johan; Moseid, Kine Onsum; Nummelin, Aleksi; Tang, Hui; Zhang, Zhongshi; Heinze, Christoph; Iversen, Trond; Schulz, Michael (2020b). *NCC NorESM2-LM model output prepared for CMIP6 C4MIP 1pctCO₂-bgc* (Version 20220602). Earth System Grid Federation. <https://doi.org/10.22033/ESGF/CMIP6.13724>

Takemura, T., Nozawa, T., Emori, S., Nakajima, T. Y., and Nakajima, T. (2005). Simulation of climate response to aerosol direct and indirect effects with aerosol transport-radiation model, *J. Geophys. Res.*, 110, D02202, doi:10.1029/2004JD005029

Tang, Y., Walton, J., Woodward, S., and Yool, A. (2020). Description and evaluation of aerosol in UKESM1 and HadGEM3-GC3.1 CMIP6 historical simulations, *Geosci. Model Dev.*, 13, 6383–6423, <https://doi.org/10.5194/gmd-13-6383-2020>

Tang, Y., Rumbold, S., Ellis, R., Kelley, D., Mulcahy, J., Sellar, A., Walton, J., & Jones, C. (2019a). MOHC UKESM1.0-LL model output prepared for CMIP6 CMIP 1pctCO₂ (Version 20220602) [Application/x-netcdf]. Earth System Grid Federation. <https://doi.org/10.22033/ESGF/CMIP6.5792>

Tang, Y., Rumbold, S., Ellis, R., Kelley, D., Mulcahy, J., Sellar, A., Walton, J., & Jones, C. (2019b). MOHC UKESM1.0-LL model output prepared for CMIP6 CMIP piControl (Version 20220602) [Application/x-netcdf]. Earth System Grid Federation. <https://doi.org/10.22033/ESGF/CMIP6.6298>

Tang, Y., Rumbold, S., Ellis, R., Kelley, D., Mulcahy, J., Sellar, A., Walton, J., & Jones, C. (2019c). MOHC UKESM1.0-LL model output prepared for CMIP6 CMIP abrupt-4xCO₂ (Version 20220602) [Application/x-netcdf]. Earth System Grid Federation.
<https://doi.org/10.22033/ESGF/CMIP6.5843>

Tatebe, H., Ogura, T., Nitta, T., Komuro, Y., Ogochi, K., Takemura, T., Sudo, K., Sekiguchi, M., Abe, M., Saito, F., Chikira, M., Watanabe, S., Mori, M., Hirota, N., Kawatani, Y., Mochizuki, T., Yoshimura, K., Takata, K., O’ishi, R., ... Kimoto, M. (2019). Description and basic evaluation of simulated mean state, internal variability, and climate sensitivity in MIROC6. *Geoscientific Model Development*, 12(7), 2727–2765.
<https://doi.org/10.5194/gmd-12-2727-2019>

Tatebe, H., & Watanabe, M. (2018a). MIROC MIROC6 model output prepared for CMIP6 CMIP 1pctCO₂ (Version 20220621) [Application/x-netcdf]. Earth System Grid Federation. <https://doi.org/10.22033/ESGF/CMIP6.5371>

Tatebe, H., & Watanabe, M. (2018b). MIROC MIROC6 model output prepared for CMIP6 CMIP piControl (Version 20220621) [Application/x-netcdf]. Earth System Grid Federation. <https://doi.org/10.22033/ESGF/CMIP6.5711>

Tatebe, H., & Watanabe, M. (2018c). MIROC MIROC6 model output prepared for CMIP6 CMIP abrupt-4xCO₂ (Version 20220621) [Application/x-netcdf]. Earth System Grid Federation. <https://doi.org/10.22033/ESGF/CMIP6.5411>

Tegen, I., Neubauer, D., Ferrachat, S., Siegenthaler-Le Drian, C., Bey, I., Schutgens, N., Stier, P., Watson-Parris, D., Stanelle, T., Schmidt, H., Rast, S., Kokkola, H., Schultz, M., Schroeder, S., Daskalakis, N., Barthel, S., Heinold, B., & Lohmann, U. (2019). The global aerosol–climate model ECHAM6.3–HAM2.3 – Part 1: Aerosol evaluation. *Geoscientific Model Development*, 12(4), 1643–1677. <https://doi.org/10.5194/gmd-12-1643-2019>

Terrenoire, E., Hauglustaine, D., Cohen, Y., Cozic, A., Valorso, R., Lefèvre, F., and Matthes, S. (2022). Impact of present and future aircraft NO_x and aerosol emissions on atmospheric composition and associated direct radiative forcing of climate, *Atmos. Chem. Phys. Discuss. [preprint]*, <https://doi.org/10.5194/acp-2022-222>, in review

Thornhill, G., Collins, W., Olivié, D., Skeie, R. B., Archibald, A., Bauer, S., Checa-Garcia, R., Fiedler, S., Folberth, G., Gjermundsen, A., Horowitz, L., Lamarque, J.-F., Michou, M., Mulcahy, J., Nabat, P., Naik, V., O'Connor, F. M., Paulot, F., Schulz, M., Scott, C. E., Séférian, R., Smith, C., Takemura, T., Tilmes, S., Tsigaridis, K., and Weber, J. (2021). Climate-driven chemistry and aerosol feedbacks in CMIP6 Earth system models, *Atmos. Chem. Phys.*, 21, 1105–1126, <https://doi.org/10.5194/acp-21-1105-2021>

Turnock, S. T., Allen, R. J., Andrews, M., Bauer, S. E., Deushi, M., Emmons, L., Good, P., Horowitz, L., John, J. G., Michou, M., Nabat, P., Naik, V., Neubauer, D., O'Connor, F. M., Olivié, D., Oshima, N., Schulz, M., Sellar, A., Shim, S., Takemura, T., Tilmes, S., Tsigaridis, K., Wu, T., and Zhang, J. (2020). Historical and future changes in air pollutants from CMIP6 models, *Atmos. Chem. Phys.*, 20, 14547–14579, <https://doi.org/10.5194/acp-20-14547-2020>

Yukimoto, S., Koshiro, T., Kawai, H., Oshima, N., Yoshida, K., Urakawa, S., Tsujino, H., Deushi, M., Tanaka, T., Hosaka, M., Yoshimura, H., Shindo, E., Mizuta, R., Ishii, M., Obata, A., & Adachi, Y. (2019a). MRI MRI-ESM2.0 model output prepared for CMIP6 CMIP 1pctCO₂ (Version 20220602) [Application/x-netcdf]. Earth System Grid Federation. <https://doi.org/10.22033/ESGF/CMIP6.5356>

Yukimoto, S., Koshiro, T., Kawai, H., Oshima, N., Yoshida, K., Urakawa, S., Tsujino, H., Deushi, M., Tanaka, T., Hosaka, M., Yoshimura, H., Shindo, E., Mizuta, R., Ishii, M., Obata, A., & Adachi, Y. (2019b). MRI MRI-ESM2.0 model output prepared for CMIP6 CMIP piControl (Version 20220602) [Application/x-netcdf]. Earth System Grid Federation. <https://doi.org/10.22033/ESGF/CMIP6.6900>

Yukimoto, S., Koshiro, T., Kawai, H., Oshima, N., Yoshida, K., Urakawa, S., Tsujino, H., Deushi, M., Tanaka, T., Hosaka, M., Yoshimura, H., Shindo, E., Mizuta, R., Ishii, M., Obata, A., & Adachi, Y. (2019c). MRI MRI-ESM2.0 model output prepared for CMIP6 CMIP abrupt-4xCO₂ (Version 20220602) [Application/x-netcdf]. Earth System Grid Federation. <https://doi.org/10.22033/ESGF/CMIP6.6755>

Yukimoto, S. et al (2019d). The meteorological research institute earth system model version 2.0, MRI-ESM2.0: description and basic evaluation of the physical component. *J. Meteor. Soc. Japan*, 97, 931–65, <https://doi.org/10.2151/jmsj.2019-051>

Zhao, X., Allen, R. J., & Thomson, E. S. (2021). An implicit air quality bias due to the state of pristine aerosol. *Earth's Future*, 9, e2021EF001979. <https://doi.org/10.1029/2021EF001979>